Supplementary information for:

Design, characterization, and first field deployment of a novel aircraft-based aerosol mass spectrometer combining the laser ablation and flash vaporization techniques

Andreas Hünig[1,2], Oliver Appel[1,2], Antonis Dragoneas[1,2], Sergej Molleker[1,2], Hans-Christian Clemen[2], Frank Helleis[2], Thomas Klimach[2], Franziska Köllner[1], Thomas Böttger[2], Frank Drewnick[2], Johannes Schneider[2], and Stephan Borrmann[1,2]

[1]Institute for Atmospheric Physics, Johannes Gutenberg University, Mainz, Germany
[2]Max Planck Institute for Chemistry, Mainz, Germany

S1 Instrument design

S1.1 Three-dimensional drawing and photographs of the ERICA

To visualize the orientation of the major components, Fig. S1 shows a three-dimensional drawing of the instrument body including the TMPs in dark red. The particle entry includes the CPI (dark green) which is mounted to the aerodynamic lens (ADL; bright red) that intrudes into the detection unit recipient (light gray). The detection laser units (orange) are oriented perpendicular (y-direction) to the particle beam (z-direction) and to the PMTs (dark blue, x-direction). The ablation laser head (black) is mounted on top of the B-ToF-MS (light blue) and emits the laser beam towards a dichroitic mirror that reflects the laser beam in the same direction as the detection lasers (-y-direction). A plano-convex lens focuses the laser beam on the particle beam. Hence, all lasers are oriented parallel onto the particle beam. The shutter unit (SU; purple) of the ERICA-AMS is located between the B-ToF-MS and the ionizer chamber of the ERICA-AMS (yellow). The C-ToF-MS (light green) protrudes over the B-ToF-MS (light blue). Fig. S2 shows photographs of the ERICA.
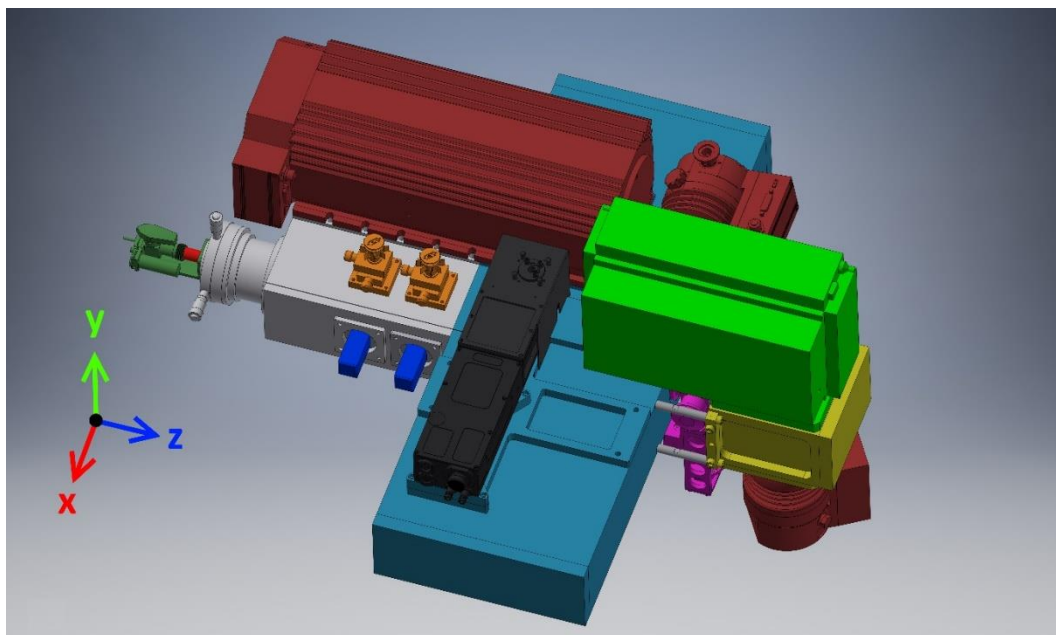
Fig. S1: Three-dimensional drawing of the instruments body showing the major components of the ERICA-LAMS and the ERICA-AMS color coded (see text). The three-dimensional drawings of the turbo molecular pumps (dark red; Pfeiffer Vacuum GmbH, Germany) and the ablation laser head (black; Quantel, France) were provided by the manufacturers.
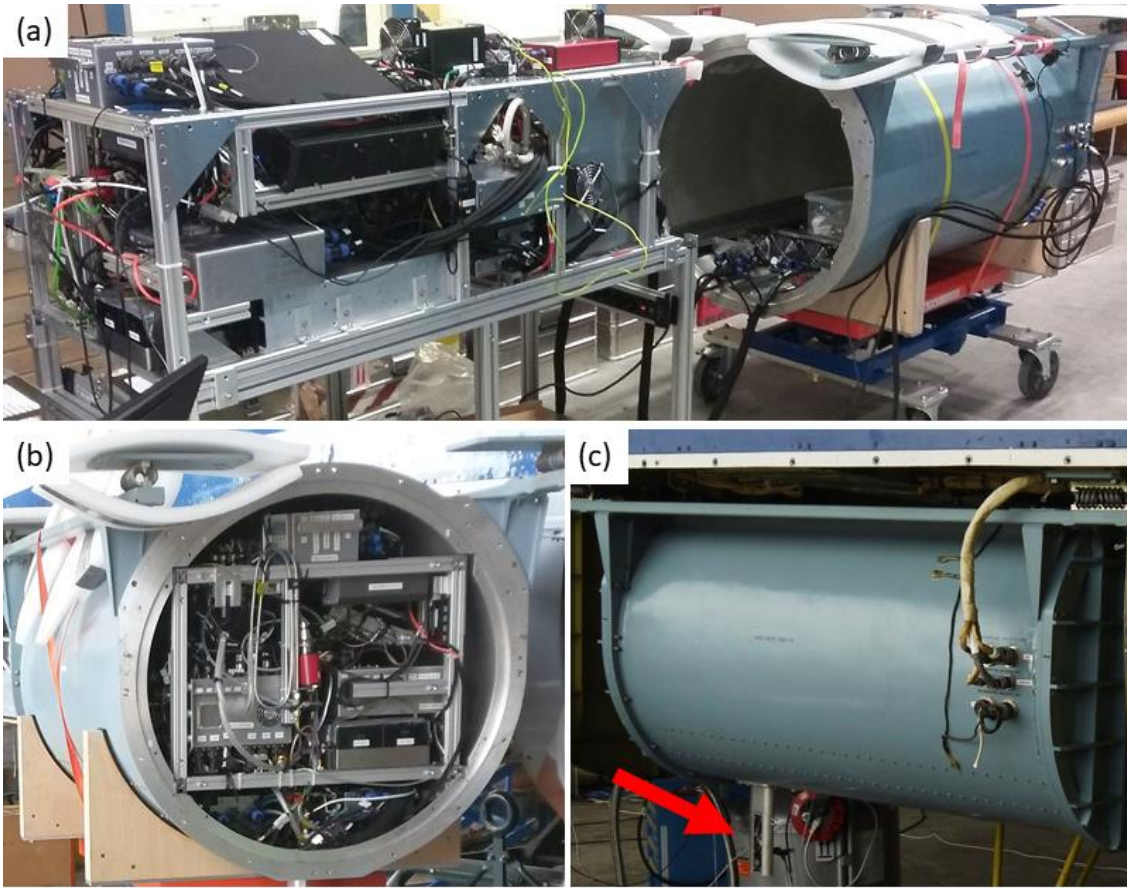
Fig. S2: (a) ERICA mounted in the rack for the StratoClim campaign outside of the container for deployment aboard the M-55 *Geophysica* (Dragoneas et al., 2021). (b) ERICA inside the container with opened front lid. (c) ERICA inside the container with closed lids and mounted on the aircraft. The shaft of the inlet for sampling the ambient air can be seen protruding at the bottom left of the container (red arrow).

S1.2   Geometry and distance ratios in the ERICA

The parameters r_{eff}, σ, and x_0 were determined by Eqs. (5), (S14), and (S16) and are thus in the dimension relative to the ADL position x_{pos}. For the graphics and the calculations in Sect. 3.3.2 and 3.3.3, the parameters were rescaled to the dimension of the particle beam at the specific location (PDU1, PDU2, ablation point, and ERICA-AMS vaporizer) by the intercept theorem. Table S1 shows these factors according to the distances in the ERICA (see Fig. S3). The pulse generator multiplier (see Sect. 2.4) value of the TC is based on the ratio of the PDU2-ablation spot distance to the PDU1-PDU2 distance and can be calculated to $\frac{120{,}7\ mm}{66{,}5\ mm} = 1.815$.

In Fig. S3, the red arrows indicate the directions of the movement of the lens and the particle beam during an ADL position scan in x-direction (using the ball joint as pivot).

Table S1: Factors to rescale the parameters $r_{eff,L}$, $r_{eff,V}$, σ, and x_0 to the dimension of the particle beam at the specific location: PDU1, PDU2, ablation point, and ERICA-AMS vaporizer.

Location	Factor
PDU1	$\frac{58.8\ mm}{133.7\ mm} = 0.44$
PDU2	$\frac{58.8\ mm + 66.5\ mm}{133.7\ mm} = 0.937$
ablation point	$\frac{246\ mm}{133.7\ mm} = 1.840$
vaporizer	$\frac{547.3\ mm}{133.7\ mm} = 4.093$
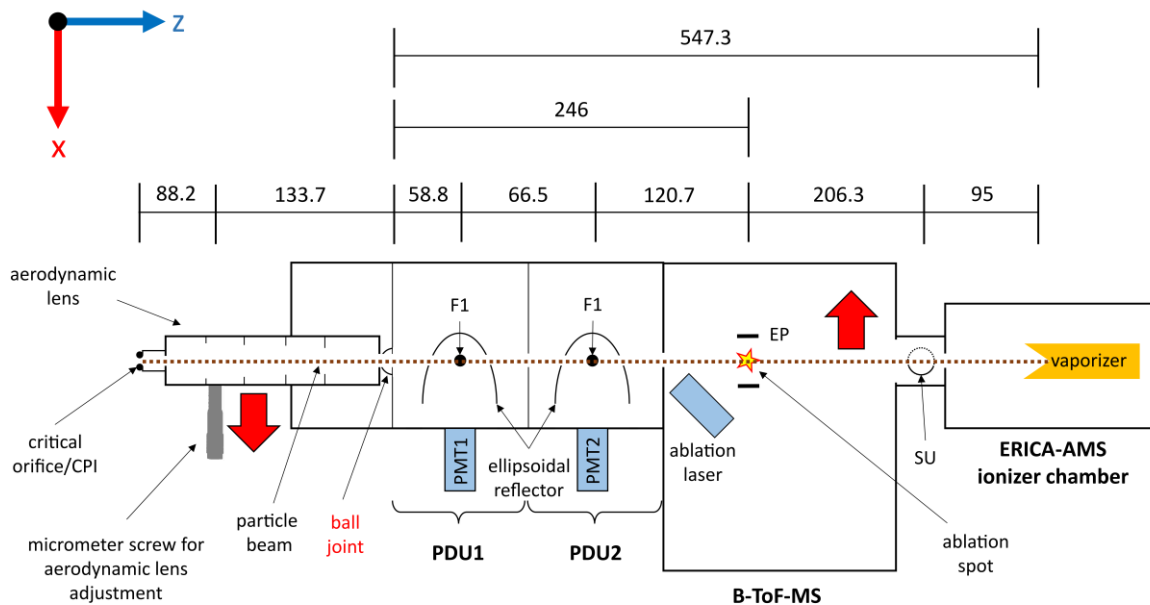
Fig. S3: Scheme of the geometry and relevant distances (in mm) along the particle beam axis in the ERICA (not to scale; see also Fig. 1). The red arrows indicate the directions of the movement of the lens and the particle beam during a scan with the ADL in x-direction. F1 is the focal point of the ellipsoidal reflector (compare Fig. S4).

S1.3   Design of the ellipsoidal reflectors

The first elliptical focal point F1 of the reflector is adjusted to coincide with the axis of the particle beam as well as with the focal point of the laser unit. At its open end, the reflector has an inner diameter of 50.8 mm and the distance between the ellipsoid's two foci is 49.78 mm. Four openings allow the laser beam and the perpendicularly incoming particle beam to pass through the reflectors. Fig. S4a shows the ellipsoidal reflector including the taper angles (blue, green, and red taper) not contributing to the scattered light signal recorded by the PMT, i.e., only light that is reflected on the reflector surface (yellow) is collected in F2. Thus, light that is scattered into a taper angle of 180° to 164.8° and 14.0° to 0° with respect to the laser beam axis (y-axis, green taper) and into a taper angle of 180° to 175° and 5.0° to 0° with respect to the particle beam axis (z-axis, blue taper) is not detected. In addition, scattered light that is emitted in a taper angle of 44.4° with respect to the F1-F2 axis (x-axis, red taper) is not reflected by the ellipsoidal reflector and thus not detected (see example Beam B3 in Fig. S4b). At F2, a spatial filter with an aperture of 0.2 mm diameter is positioned such that the light scattered from the particles is separated from the background light.
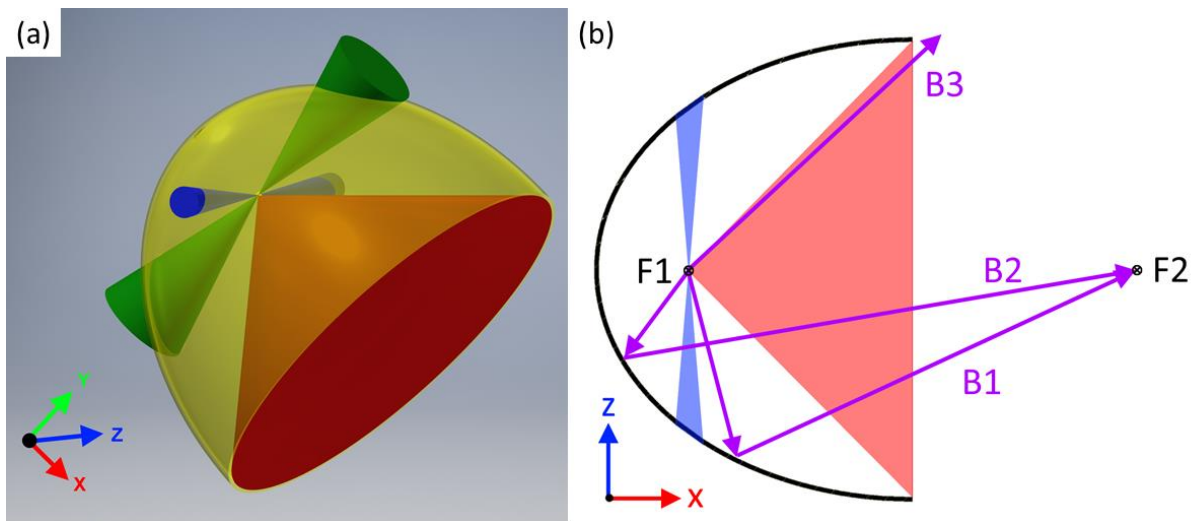
Fig. S4: Left: Three-dimensional drawing of the ellipsoidal reflector (semi-transparent yellow) including the taper angle ranges (blue, green, and red; see text) not contributing to the scattered light signal recorded by the PMT. **Right:** Scheme of the ellipsoidal reflector in the xz-plane with various beam paths of light scattered by a particle. The beams B1 and B2 are reflected to F2 and thus detected by the PMT, beam B3 is not detected.

S2   Laser characterization

The detection and ablation laser beam waists were determined by a knife edge experiment. For this, a razor blade was moved stepwise perpendicularly into the respective laser beam and the remaining energy was measured (see Sect. 3.1).

S2.1   Characterization of the detection lasers

5   Fig. S5 shows the plots of the measurements of the knife edge experiment at the detection laser beam (see Sect. 3.1 and caption for further details).
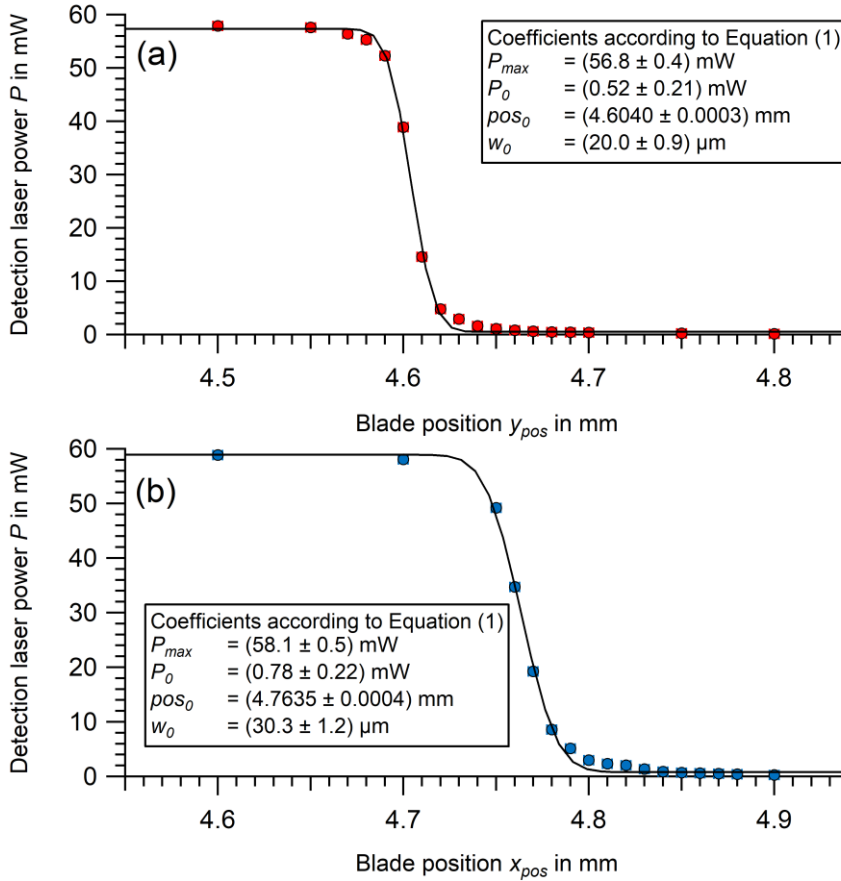
Fig. S5: Detection laser beam characterization measurement in the focal point of the optical setup (x-direction: panel a, y-direction: panel b) curve fitted with Eq. (1), where P is the measured power, P_0 is the offset of the power for the fitting routine baseline
10   **subtraction, P_{max} the Gaussian area of the intensity profile, pos_0 the central point, pos the horizontal position of the blade, and $w_{0,rad}$ the beam waist radius (1/e²-radius) of the Gaussian profile in focal point. The uncertainties of the detection laser power P reflect the fluctuation of the value at the bolometer display and the uncertainty of the blade position (x_{pos} and y_{pos}) is based on the reading error of the micrometer positioning system. The uncertainty bars are smaller than the symbols. The text boxes display the values and uncertainties of the parameters from the curve fitting.**

S2.2 Characterization of the ablation laser focus

In order to determine the characteristic parameters of the ablation laser focus, the knife edge experiment is conducted at eight different positions along the laser beam's optical axis. Fig. S6 shows the plot of the measurements for the ablation laser beam (see Sect. 3.1 and caption for further details).
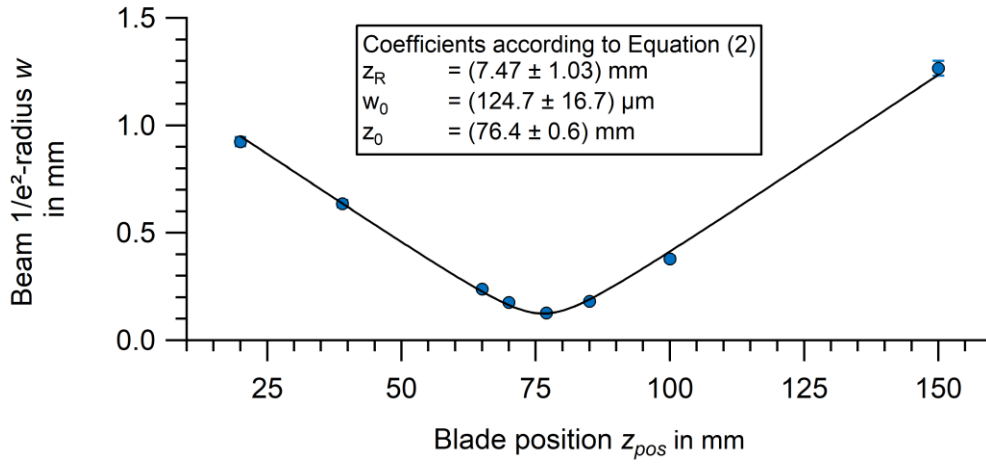
Fig. S6: Ablation laser beam characterization along the laser beam axis by curve fitting with Eq. (2), where z_R is the Rayleigh range, z_0 the focal length, and $w_{0,rad}$ is the beam waist radius ($\frac{1}{e^2}$ −radius). The uncertainties of the ablation laser energy E reflect the fluctuation of the value at the energy meter display and the uncertainty of the blade position z_{pos} is based on the reading error of
10 **the used caliper. The uncertainty bars are smaller than the symbols. The text box displays the values and uncertainties of the parameters from the curve fitting.**

S3   Experimental setup for laboratory experiments and deployed particle sizes

For clarity of the description in the paper, the three straightforward particle generation setups are depicted in Fig. S7. Out of a salt solution or polystyrene latex NIST particle size standard (PSL; Polysciences Europe GmbH, Germany) suspension the particles were created in a nebulizer (TSI 3076, TSI Inc., St. Paul, Minnesota, USA). For the PSL size calibration the aerosol
5 was directed through two silica gel (orange gel, Carl Roth GmbH & Co. KG, Germany) diffusion dryers into ERICA (Setup A in Fig. S7). The particle sizes used are listed in Table S2. All the ammonium nitrate (AN; Merck KGaA, Germany) particles (Table S3) and the PSL particles for the particle beam characterization by the ADL position scan (see Sect. 3.3; Table S4) were additionally charge neutralized by a X-ray bipolar charger (TSI 3012, TSI Inc., St. Paul, Minnesota, USA) and size selected by a differential mobility analyzer (DMA, Minnesota Type 5.5-900, GRIMM Aerosol Technik Ainring GmbH & Co.
10 KG, Germany). After passing the DMA, the aerosol output is split into two lines. One line to ERICA and the other to a condensation particle counter (CPC, Series 5.400 CPC, GRIMM Aerosol Technik Ainring GmbH & Co. KG, Germany) for number concentration measurements (Setup B in Fig. S7). Setup C (Fig. S7) refers to the case, where an OPC was used as a reference device (see Table S2).

The measurements with the OPC were conducted only with PDU1 to reduce measurement time and were adopted from
15 Molleker et al. (2020). During these measurements, the thresholds at PMT1 were adjusted (increasing with particle size) to filter the particle signal from signals caused by residual particle fragments in the PSL suspension. Thus, the parameter $r_{eff,L}$ (see Sect. 3.3.2) is somewhat underestimated for these measurements. Also, the measurements with the OPC were conducted after the particle time-of-flight calibration and particle beam characterization measurements with the CPC as a reference device. Before the measurements with the OPC could be performed, the ADL was accidentally re-installed rotated by about
20 90°. Since the overall particle beam cross-sectional area does not describe a circle but an oval shape (Hünig, 2021), the rotation of the ADL might partially influence the results. However, we assume that the parameters $r_{eff,L}$, $r_{eff,V}$, σ, and A_{scan} are only slightly dependent on the rotation angle of the lens. Thus, they are included in the graphics (see Sect. 3.3) to extend the measurement range, despite being not fully comparable. The parameter x_0 seems to be more dependent on the rotation angle (see Sect. S4.6.2). Thus, x_0 for the OPC measurements is not presented in Fig. 10 and Fig. S13. However, the ADL was rotated
25 after the field deployment in Kathmandu, Nepal (see Sect. 4). Thus, the characterization measurements with the CPC in Sect. 3.3 reflect the conditions during the field deployment.
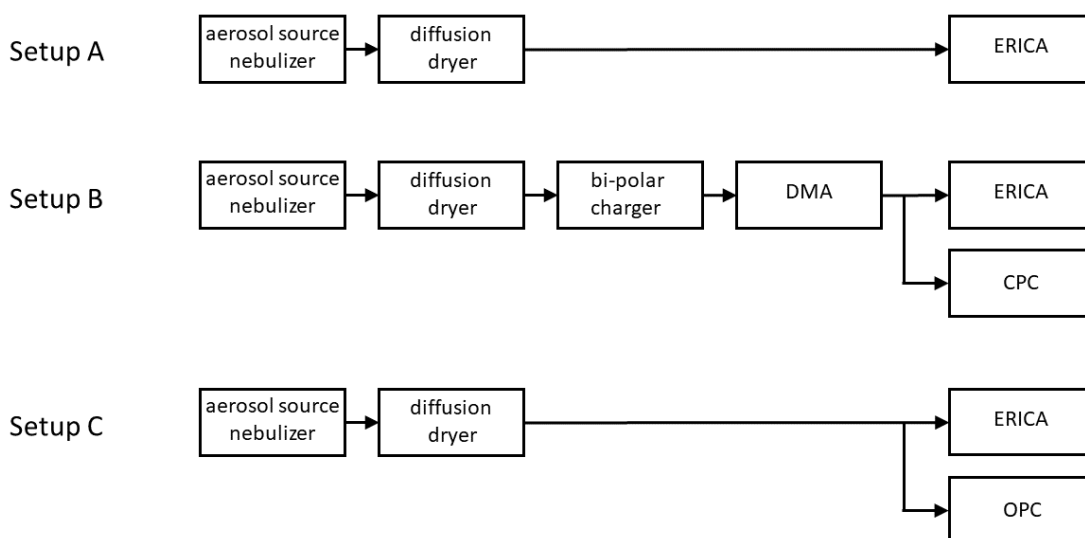
Fig. S7: Scheme of the measurement setups A, B, and C for the characterization measurements.

For further laboratory studies (see Sect. 3.5.1) also solutions of sodium chloride (Merck KGaA, Germany) and benz[a]anthracene (Sigma-Aldrich, Inc., USA), as well as a suspension of gold spheres (Sigma-Aldrich, Inc., USA; d_{va} = 3860 nm; geometric diameter d_{geo} = 200 nm) were nebulized. Here, Setup A (see Fig. S7) was used.

5   For proper concurrent operation of ERICA-LAMS and ERICA-AMS, the axial orientation of the ADL with two degrees of freedom first needs to be centered and adjusted (using AN particles) such that the particle beam actually hits the AMS vaporizer. Afterwards, the other foci from the two PDU lasers and the ellipsoidal reflectors, as well as the ablation laser optics need to be adjusted to the particle beam axis. Considering the stability requirements for aircraft operation (including flight through convective cloud outflows), this is a tedious, difficult, and time-consuming procedure with correspondingly high
10 demands on the design and tolerances of the mechanical components as well as on the operator's skills.

For the PSL particles the vacuum aerodynamic diameter d_{va} is calculated from the NIST certified geometric diameter d_{geo} assuming a PSL density ρ_{PSL} = 1.05 g cm^{-3}, and the unit density ρ_o = 1 g cm^{-3} (Hinds, 1999; Jimenez et al., 2003a, b; DeCarlo et al., 2004):

$$d_{va} = d_{geo} \cdot \frac{\rho_{PSL}}{\rho_o} \tag{S1}$$

15 For the particle beam characterization measurements, a different set of PSL sizes (d_{va}) was used (see Table S4). Here, the d_{va} was calculated from the selected electric mobility particle diameter d_{mob} to which the DMA was set (DeCarlo et al., 2004):

$$d_{va} = d_{mob} \cdot \frac{\rho_{PSL}}{\rho_o} \tag{S2}$$

AN (Merck KGaA, Germany) particles are detectable with the ERICA-LAMS as well as the ERICA-AMS units (particle sizes see Table S3). To calculate d_{va} from d_{mob} (to which the DMA was set) the particle density ρ_{AN} was assumed to be 1.725 g cm^{-3} (Zapp et al., 2000) and the Jayne shape factor S to be 0.8 (Jayne et al., 2000).

$$d_{va} = d_{mob} \cdot S \cdot \frac{\rho_{AN}}{\rho_o} \tag{S3}$$

20 Table S2 lists the PSL NIST particle size standards used for particle time-of-flight calibration measurements in Sect. 3.2 and adjustment measurements. Listed are the particle sizes in geometric diameters d_{geo} (NIST certified). The vacuum aerodynamic diameters d_{va} were calculated from d_{geo}. Also, the purpose of the application is provided (labelled as X).

Table S2: Measured PSL NIST size standards for particle size calibration measurements and particle beam characterization measurements. Listed are the particle sizes in geometric diameters d_{geo} (NIST certificate), their absolute uncertainties $\Delta^{abs}d_{geo}$, the calculated vacuum aerodynamic diameters d_{va}, and absolute $\Delta^{abs}d_{va}$ and relative uncertainties $\Delta^{rel}d_{va}$.

PSL particle sizes					Used for	
d_{geo} in nm	$\Delta^{abs}d_{geo}$ in nm	d_{va} in nm	$\Delta^{abs}d_{va}$ in nm	$\Delta^{rel}d_{va}$ in %	Size calibration	Particle beam characterization with OPC
76	11	80	11	14	X	
100	5	105	5	5	X	
150	9	158	9	6	X	
198	7	207	8	3.7	X	
288	14	302	15	5	X	
356	14	374	15	4	X	
401	12	421	13	3	X	
599	10	629	11	1.7	X	
794	24	834	25	3	X	X
990	30	1040	31	3	X	X
1540	39	1617	40	2.5	X	X
1990	60	2090	63	3	X	X
2580	65	2709	68	2.5	X	X
3000	60	3150	63	2	X	X
4900	25	5145	26	0.5	X	

5 Table S3 lists the AN particle sizes used for particle time-of-flight calibration measurements in Sect. 3.2 and particle beam properties measurements (parameters: $r_{eff,L}$, $r_{eff,V}$, σ, x_0, and A_{scan}) in Sect. 3.3. The uncertainty of AN particle size d_{va} is estimated to be 3 % (Hings, 2006).

Table S3: AN particle sizes used for size calibration measurements, particle beam characterization measurements and ADL adjustment. Listed are the particle sizes in electric mobility particle diameters d_{mob} and the calculated vacuum aerodynamic diameters d_{va}. The uncertainty of all sizes is estimated to be 3 %. X*: results useable for evaluation of DE_{AMS} at the ERICA-AMS vaporizer only. X: results useable for evaluation of DE_{AN} at the PDUs only.**

AN particle diameter		Used for	
d_{va} in nm	d_{mob} in nm	Size calibration	Particle beam characterization and detection efficiency determination with DMA
91	66		X*
138	100	X	X*
177	128	X	
213	154	X	X
276	200	X	
297	215	X	X
335	243	X	X
483	350	X	X**
548	397	X	X**
814	590	X	X**

Table S4 lists the PSL NIST particle size standards used for particle beam properties measurements (parameters: $r_{eff,L}$, σ, x_0, and A_{scan}) in Sect. 3.3. Listed are the particle sizes in geometric diameter d_{geo} (NIST certificate) and in vacuum aerodynamic diameter d_{va}, calculated from the set electric mobility diameter d_{mob}.

Table S4: PSL NIST size standards for particle beam characterization measurements. Particle sizes in electric mobility particle diameters d_{mob}, geometric diameters d_{geo} (NIST certificate), absolute uncertainties $\Delta^{abs} d_{geo}$, the calculated vacuum aerodynamic diameters d_{va}, and absolute $\Delta^{abs} d_{va}$ and relative uncertainties $\Delta^{rel} d_{va}$. Also, the electric mobility diameters values d_{mob} to which the DMA was set are listed.

d_{geo} in nm	$\Delta^{abs} d_{geo}$ in nm	d_{va} in nm	$\Delta^{abs} d_{va}$ in nm	$\Delta^{rel} d_{va}$ in nm	d_{mob} in nm
103	14	108	15	14	105
208	7	218	8	4	225
390	12	410	13	3	405
599	12	629	13	2	585
794	27	834	28	3	795

Fig. S8 shows the histograms of the PSL calibration measurements (Sect. 3.2), where the different sizes can be clearly distinguished. Only the peak of the PSL particles with 105 nm in size overlaps with that of the measurement of the PSL particles with 80 nm in size. In order to find the center of the peaks, which were used as upc value for calibration, a Gaussian distribution curve was fitted to the individual histograms in Fig. S8.
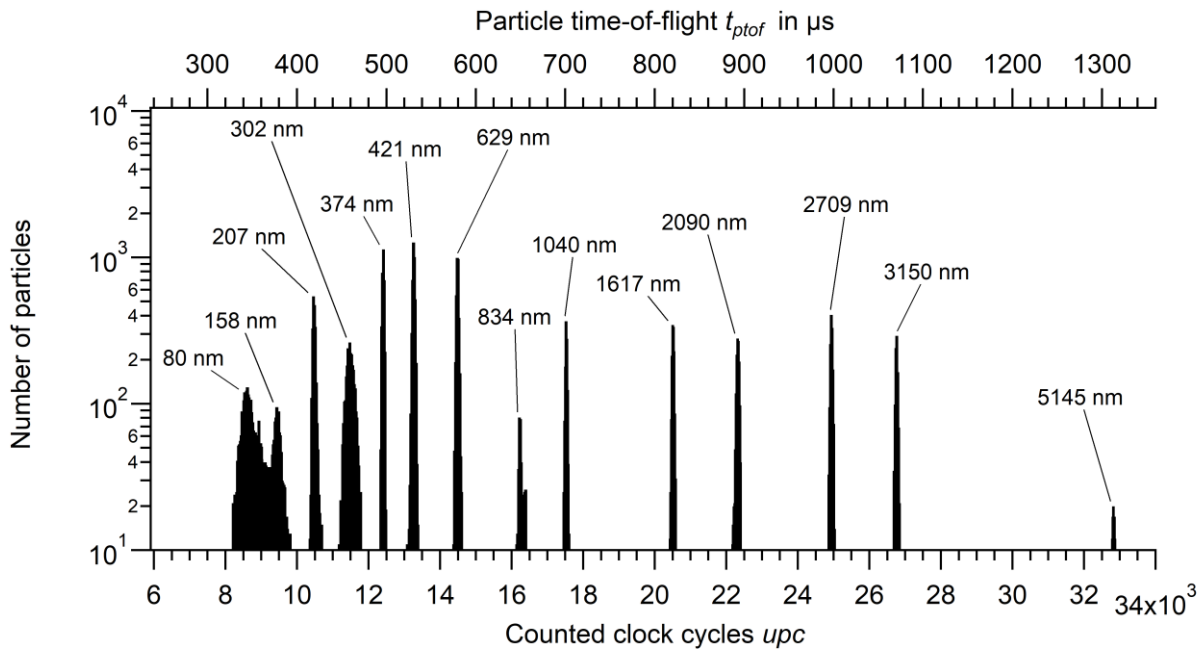
Fig. S8: Combined histograms of the PSL calibration measurements (particle sizes are expressed as d_{va}). The particle flight time t_{ptof} (top abscissa) was calculated from the counted clock cycles (40 ns per cycle; bottom abscissa). The peak of d_{va} = 105 nm particles overlaps with the broad peak of d_{va} = 80 nm particles and is not visible in the graph.

S4   Particle detection efficiency

S4.1   Calculation of the relative Mie scattered light intensity

For the measurement with PSL particles of 108 nm in size, the parameter $r_{eff,L}$ could not be determined by the combined curve-fitting procedure, due to losses between PDU1 and PDU2 (see Sect. 3.3.1). The combined curve-fitting for the measurements with AN particles of 138 nm in size yielded unreasonably high values for both PDUs despite the seemingly reasonable curve progression. (see Sect. S4.2). However, $r_{eff,L}$ alternatively can be determined by means of the relative Mie scattered light intensity.

S4.1.1   Calculation of the effective laser radius for PSL particles of d_{va} = 108 nm in size

As described in Sect. 3.3.1, the curve fitting of the measurement with PSL particles of d_{va} = 108 nm (d_{geo} = (103 ± 14) nm) was not performed by the combined curve-fitting procedure, i.e., the parameter A_{scan} was not linked, because the large divergence of the particle beam will introduce losses at PDU2 and thus the assumption of having the same A_{scan} is not applicable. A_{scan} and $r_{eff,L}$ strongly correlate already for PDU1. Thus $r_{eff,L}$ has to be kept fixed at a value acquired using Mie Theory of light scattering. This was evident from the fact that the combined curve-fitting procedure of the measurement does not converge with respect to $r_{eff,L}$ and A_{scan}. The relative Mie scattered light intensity I_{rel} was calculated (Bohren and Huffman, 1998) by means of the program "BH-Mie-Rechner" programmed by Vetter (2004). Here, the wavelength of the used detection laser (λ = 405 nm) and the refractive index for PSL particles n_{PSL} of approximately 1.65 (for λ = 405 nm; real part; see supplemental information of Galpin et al. (2017)) were considered. In addition, the detector angle range was considered to be 14° – 164°, the detector angle interval 1°, and the detector to particle distance 4.9 cm.

The relative Mie scattered intensity I_{rel} is the Mie scattered light intensity I_{sc} normalized to the irradiated intensity I_{ir} (Equation (S4)).

$$I_{rel} = {I_{sc}}/{I_{ir}} \qquad (S4)$$

By that, for PSL particles of d_{geo} = 104 nm a Mie scattering intensity of $I_{rel,104nm}$= 7.10·10^{-4} a.u. and for PSL particles of d_{geo} = 208 nm $I_{rel,208nm}$= 3.42·10^{-2} a.u. was calculated.

The curve fitting of the ADL position scan with PSL particles with a size of d_{geo} = 208 nm (d_{va} = 218 nm) resulted an effective laser radius $r_{eff,L}$ = 148 µm for PDU1 and $r_{eff,L}$ = 133 µm for PDU2, considering the geometry of the instrument (see Sect. S1.2). The effective laser width $r_{eff,L}$ is a multiple (by factor a_t) of the beam waist 1/e²-radius w_0 = 30.3 µm (see Sect. 3.1):

$$r_{eff,L} = a_t \cdot w_0 \qquad (S5)$$

The factor a_t is in average (mean of $a_{t,208nm}$ at PDU1 and $a_{t,208nm}$ at PDU2) $a_{t,208nm}$ = 4.687 for PSL particles with a size of d_{geo} = 208 nm. The radius r is the radius at the limit of detection $r_{eff,L}$ ($r = r_{eff,L}$).

The detection limit is the same for both particle sizes:

$$I_{sc,208nm} = I_{sc,104nm} \qquad (S6)$$

As follows from Equation (S4) and (S6)

$$I_{ir,208nm}(r_{208nm}) \cdot I_{rel,208nm} = I_{ir,104nm}(r_{104nm}) \cdot I_{rel,104nm} \qquad (S7)$$

Considering a Gaussian laser profile (Eichler et al., 2016)

$$I(r) = I_0 \cdot exp\left[-\frac{2\,r^2}{{w_0}^2}\right] \qquad (S8)$$

where r is assumed as the edge of $r_{eff,L}$ and I_0 is the intensity in the center of the laser beam. Thus, $I_{ir}(a_t)$ is the intensity at the edge of $r_{eff,L}$

$$I_{ir}(a_t) = I_0 \cdot exp[-2\,a_t{}^2] \tag{S9}$$

Inserted in Equation (S7):

$$I_{0,208nm} \cdot exp[-2\,a_{t,208nm}{}^2] \cdot I_{rel,208nm} = I_{0,104nm} \cdot exp[-2\,a_{t,104nm}{}^2] \cdot I_{rel,104nm} \tag{S10}$$

The same laser and thus the same laser intensity in the center for both particle sizes is considered by

$$I_{0,208nm} = I_{0,104nm} \tag{S11}$$

5 Solving Equation (S10) for a_{104nm}:

$$a_{t,104nm} = \sqrt{a_{t,208nm}{}^2 - \frac{1}{2}ln\left[\frac{I_{rel,208nm}}{I_{rel,104nm}}\right]} = 4.476 \tag{S12}$$

After entering the values for the calculated parameters $a_{t,208nm}$, $I_{rel,208nm}$, and $I_{rel,104nm}$ in Equation (S12), the result for factor $a_{t,104nm}$ is 4.476.

To calculate the factor $f_{Mie,104nm}$ that is used to calculate $r_{eff,L,104nm}$ out of $r_{eff,L,208nm}$, Equation (S13) is used.

$$f_{Mie,104nm} = \frac{r_{eff,L,104nm}}{r_{eff,L,208nm}} = \frac{a_{t,104nm} \cdot w_0}{a_{t,208nm} \cdot w_0} = 0.955 \tag{S13}$$

Using that determined value for $f_{Mie,104}$, the $r_{eff,L}$ value for $d_{geo} = 104$ nm ($d_{va} = 108$ nm) is $r_{eff,L} = 320\,\mu m$ at PDU1 and 10 $r_{eff,L} = 136\,\mu m$ at PDU2. The uncertainties are conservatively estimated as 4.8 µm at PDU1 and 4.0 µm at PDU2. These values are the approximated maximum uncertainties of $r_{eff,L}$ in the considered particle size range of $d_{va} = 218$ nm to $d_{va} = 834$ nm at PDU1 and PDU2. The values, shown in Fig. 6, are $r_{eff,L} = 141\,\mu m$ at PDU1 and $r_{eff,L} = 127\,\mu m$ at PDU2 with the uncertainties of 2 µm at PDU1 and 4 µm at PDU2.

S4.1.2   Calculation of the effective laser radius for AN particles of $d_{va} = 138$ nm and $d_{va} = 91$ nm in size

15 Analogous to the calculation of the factor for the determination of the $r_{eff,L}$ values for the measurement with smaller PSL particles (see Sect. S4.1.1), the factors for the measurements with AN particles with the sizes of $d_{va} = 138$ nm ($d_{geo} = 100$ nm) and $d_{va} = 91$ nm ($d_{geo} = 66$ nm) were also determined. The starting point was the $r_{eff,L}$ values of PDU1 and PDU2 determined by means of the combined curve-fitting procedure when measuring with $d_{va} = 213$ nm ($d_{geo} = 154$ nm).

The calculation of the relative Mie scattered light intensity I_{rel} was performed for different refractive indices between n = 1.30 20 and n= 1.70. The refractive index of particulate AN particles at a wavelength of $\lambda = 405$ nm is unknown but was assumed to be in that range. For the calculation of I_{rel}, the wavelength of the used detection laser ($\lambda = 405$ nm), the detector angle range of $14° - 164°$, the detector angle interval of $1°$, and the detector to particle distance of 4.9 cm was considered.

S4.1.2.1   Effective laser radius for ammonium nitrate particles of $d_{va} = 138$ nm

25 The curve fitting of the ADL position scan with AN particles of $d_{geo} = 154$ nm ($d_{va} = 213$ nm) resulted in an effective laser radius of $r_{eff,L,SC} = 89\,\mu m$ for PDU1 and $r_{eff,L,SC} = 87\,\mu m$ for PDU2, considering the geometry of the instrument (see Sect. S1.2).

The factor a_t (see Eq. (S5)) is in average (mean of $a_{t,154nm}$ at PDU1 and $a_{t,154nm}$ at PDU2) $a_{t,154nm} = 2.911$ for AN particles of $d_{geo} = 154$ nm. The beam waist $1/e^2$-radius w_0 is 30.3 µm (see Sect. 3.1). To calculate $a_{t,100nm}$, Eq. (S12) is used, where 30 $a_{t,104nm}$ is substituted by $a_{t,100nm}$, $a_{t,208nm}$ by $a_{t,154nm}$, $I_{rel,104nm}$ by $I_{rel,100nm}$, and $I_{rel,208nm}$ by $I_{rel,154nm}$. The factor $f_{Mie,100nm}$ is calculated using Eq. (S13), where $f_{Mie,104nm}$ is substituted by $f_{Mie,100nm}$, $a_{t,104nm}$ is substituted by $a_{t,100nm}$, and $a_{t,208nm}$ by $a_{t,154nm}$. The results for the various refractive indices are shown in Table S5.

Table S5: Calculated factors to calculate the $r_{eff,L}$ values for the measurement with AN particles of d_{geo} = 100 nm (d_{va} = 138 nm).

n	$I_{rel,154nm}$ in a.u.	$I_{rel,100nm}$ in a.u.	$a_{t,100nm}$	$f_{Mie,100nm}$
1.70	7.579·10⁻³	6.427·10⁻⁴	2.691	0.924
1.60	5.596·10⁻³	4.848·10⁻⁴	2.693	0.925
1.50	3.901·10⁻³	3.443·10⁻⁴	2.695	0.926
1.40	2.494·10⁻³	2.243·10⁻⁴	2.697	0.926
1.30	1.391·10⁻³	1.277·10⁻⁴	2.699	0.927

The average of the factors is $f_{Mie,100nm}$ = 0.926. Using that average factor, the $r_{eff,L,SC}$ value for d_{geo} = 100 nm (d_{va} = 138 nm) is 83 µm at PDU1 and 81 µm at PDU2 with the conservatively estimated uncertainties of 9 µm at PDU1 and 14 µm at PDU2 (see Fig. 6). These uncertainty values are the approximated maximum uncertainties in the considered size range of d_{va} = 213 nm to d_{va} = 814 nm, as determined by the curve-fitting procedure.

S4.1.2.2 Effective laser radius for ammonium nitrate particles of d_{va} = 91 nm

The calculation of the $r_{eff,L}$ for AN particles of d_{va} = 91 nm was conducted similar to the calculation of $r_{eff,L}$ for particles of d_{va} = 138 nm (see Sect. S4.1.2.1): The curve fitting of the ADL position scan with AN particles of d_{geo} = 154 nm (d_{va} = 213 nm) resulted an $r_{eff,L,SC}$ = 89 µm for PDU1 and $r_{eff,L,SC}$ = 87 µm for PDU2, considering the geometry of the instrument.

The factor a_t (see Eq. (S5)) is in average (mean of $a_{t,154nm}$ at PDU1 and $a_{t,154nm}$ at PDU2) $a_{t,154nm}$ = 2.911 for AN particles of d_{geo} = 154 nm. The beam waist 1/e²-radius w_0 is 30.3 µm (see Sect. 3.1). To calculate $a_{t,66nm}$, Eq. (S12) is used, where $a_{t,104nm}$ is substituted by $a_{t,66nm}$, $a_{t,208nm}$ by $a_{t,154nm}$, $I_{rel,104nm}$ by $I_{rel,66nm}$, and $I_{rel,208nm}$ by $I_{rel,154nm}$. The factor $f_{Mie,66nm}$ is calculated using Eq. (S13), where $f_{Mie,104nm}$ is substituted by $f_{Mie,66nm}$, $a_{t,104nm}$ is substituted by $a_{t,66nm}$, and $a_{t,208nm}$ by $a_{t,154nm}$. The results for the various refractive indices are shown in Table S6.

Table S6: Calculated factors to calculate the $r_{eff,L}$ values for the measurement with AN particles of d_{geo} = 66 nm (d_{va} = 91 nm).

n	$I_{rel,154nm}$ in a.u.	$I_{rel,66nm}$ in a.u.	$a_{t,66nm}$	$f_{Mie,66nm}$
1.70	7.579·10⁻³	5.158·10⁻⁵	2.446	0.840
1.60	5.596·10⁻³	3.968·10⁻⁵	2.450	0.841
1.50	3.901·10⁻³	2.877·10⁻⁵	2.454	0.843
1.40	2.494·10⁻³	1.914·10⁻⁵	2.458	0.844
1.30	1.391·10⁻³	1.114·10⁻⁵	2.462	0.846

The average of the factors is $f_{Mie,66nm}$ = 0.843. Using that average factor, the $r_{eff,L,SC}$ value for d_{geo} = 66 nm (d_{va} = 91 nm) is $r_{eff,L,SC}$ = 75 µm at PDU1 and $r_{eff,L,SC}$ = 73 µm at PDU2 with the uncertainties of 9 µm at PDU1 and 14 µm at PDU2 (see Fig. 6). These uncertainty values are the approximated maximum uncertainties in the considered size range of d_{va} = 213 nm to d_{va} = 814 nm, as determined by the curve-fitting procedure.

S4.2 Experimental determination of detection efficiencies for particles carrying single or double electrical charges

In addition to the particle detection efficiency for PSL particles, the detection efficiency of particle counting at both detection units PDUs was determined for AN particles (particle sizes see Table S2) according to Eq. (4). For this, a newly developed approach was adopted. An example of the AN particle measurement at the PDUs is provided in Sect. S4.4. For polydisperse

aerosol (like nebulized and dried AN), not only singly charged particles pass through the DMA, but also larger particles with higher charges having the same electric mobility Z (Allen and Raabe, 1985; Seinfeld and Pandis, 2016). Besides the singly charged (SC), the doubly charged (DC) particles have to be considered when using a DMA for size selection out of a polydisperse aerosol. The fraction of triply or higher charged particles is negligible in the investigated size range (Wiedensohler, 1988). Since the determined parameters $r_{eff,L}$, x_0, σ, and A_{scan} show a size dependency in the results of an ADL position scan, the doubly charged particles have to be taken into consideration.

Table S7 shows the measured sizes of the singly charged particles d_{va} and the sizes of the doubly charged particles $d_{va,DC}$. Each line in the table represents the sizes of the same electrical mobility Z. For example, when the voltage at the DMA is set to allow singly charged particles of 91 nm in size, a doubly charged particle fraction f_{DC} of 0.113 of AN particles of 138 nm in size will pass as well. Two series of measurements (SOM A and SOM B, Table S7) were carried out with complementary particle sizes. Within a SOM, the particle size of the species with single charge d_{va}, e.g., d_{va} = 138 nm, also corresponds to the particle size of the species with double charge $d_{va,DC}$, i.e., $d_{va,DC}$ = 138 nm, for the next smaller species with single charge d_{va}, i.e., d_{va}= 91 nm. This approach enables an iterative procedure for the following evaluation. The fraction of doubly charged particles f_{DC} depends on the particle size and the deployed nebulizer. The calculation of the used values for the singly charged fraction f_{SC} and f_{DC}, is given in Sect. S4.3. The highest fraction of doubly charged particles can be obtained for a particle size of d_{va}= 138 nm (0.123).

Table S7: Singly charged (SC) particles of sizes d_{va} and the corresponding doubly charged (DC) particles $d_{va,DC}$ with the same electrical mobility value. Provided in addition are the corresponding fractions of singly f_{SC} and doubly charged f_{DC} particles for the two series of measurements (SOM) A and B.

d_{va} singly charged (SC) particles in nm	$d_{va,DC}$ doubly charged (DC) particles in nm	f_{SC}	f_{DC}	SOM
91	138	0.887	0.113	A
138	213	0.877	0.123	
213	335	0.892	0.108	
335	548	0.937	0.063	
548	934	1.000	0.000	
297	483	0.964	0.036	B
483	814	0.982	0.018	
814	1435	1.000	0.000	

In order to incorporate the doubly charged particles during the curve-fitting, Eq. (5) was extended by a term for the doubly charged particles to form Eq. (S14). The parameters subscripted with SC refer to the singly charged particles, the parameters subscripted with DC refer to the doubly charged particles:

$$DE_{AN}(x_{pos}) =$$

$$\left(\frac{1}{2} \cdot \left(erf\left(\frac{x_{pos} + r_{eff,L,SC} - x_{0,SC}}{\sqrt{2}\ \sigma_{SC}}\right) - erf\left(\frac{x_{pos} - r_{eff,L,SC} - x_{0,SC}}{\sqrt{2}\ \sigma_{SC}}\right)\right) \cdot A_{scan,SC} \cdot f_{SC}\right) \quad (S14)$$

$$+ \left(\frac{1}{2} \cdot \left(erf\left(\frac{x_{pos} + r_{eff,L,DC} - x_{0,DC}}{\sqrt{2}\ \sigma_{DC}}\right) - erf\left(\frac{x_{pos} - r_{eff,L,DC} - x_{0,DC}}{\sqrt{2}\ \sigma_{DC}}\right)\right) \cdot A_{scan,DC} \cdot f_{DC}\right)$$

The parameters were determined iteratively with the procedure outlined in Fig. S9. The iteration series was started at the largest particle size in the respective SOM (A or B). For SOM A this is 548 nm, for SOM B it is 814 nm. For the first iteration, f_{DC} = 0 is assumed in each case, since it based on the fact that particles larger than 1000 nm ($d_{va,DC}$) are delivered by the aerosol

generator. Then, in analogy to the procedure for the measurements with PSL particles, a combined curve-fitting, here for AN with Eq. (S14), was carried out. The parameters $x_{0,SC}$, σ_{SC}, $r_{eff,L,SC}$, and $A_{scan,SC}$ obtained in each case are used in the next iteration step as constants for the doubly charged species as $x_{0,DC}$, σ_{DC}, $r_{eff,L,DC}$, and $A_{scan,DC}$.

Example for SOM A: For the combined curve-fitting, the constants for f_{SC} and f_{DC} in Eq. (S14) are used separately for both PDUs. The first iteration starts with AN particles of 548 nm in size. According to Table S7, the second half of the term in Eq. (S14) then is zero. The variables $x_{0,SC}$, σ_{SC}, $r_{eff,L,SC}$, and $A_{scan,SC}$ obtained from this iteration are used as constants $x_{0,DC}$, σ_{DC}, $r_{eff,L,DC}$, and $A_{scan,DC}$ for the second iteration for the measurement at particle size of 335 nm. The iteration series of SOM A ends with the measurement of AN particles of 91 nm in size.
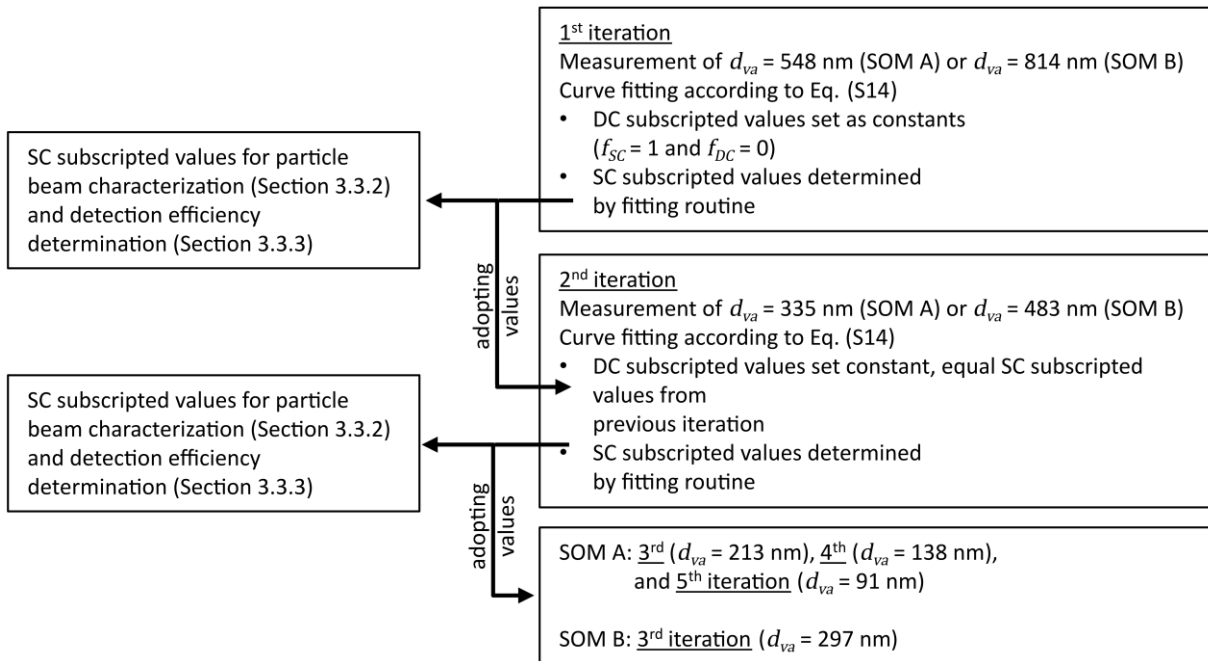
Fig. S9: Iteration scheme for SOM A and SOM B using Eq. (S14) for the combined curve-fitting. SC: Singly Charged; DC: Doubly Charged.

The combined curve-fitting for the measurements with AN particles of 138 nm in size yielded unreasonably high values for both PDUs despite the seemingly reasonable curve progression. Therefore, an approach analogous to the measurements with PSL particles with a size of 108 nm was applied (see Sect. S4.1.2). Based on known $r_{eff,L,SC}$ values at PDU1 and PDU2 for the measurements with AN particles of 213 nm, the $r_{eff,L,SC}$ values for the measurements with AN particles of 138 nm were calculated by a factor using the relative intensity of Mie scattering. A new combined curve-fitting (fourth iteration of SOM A, see Fig. S9) yielded values for $x_{0,SC}$, σ_{SC}, and $A_{scan,SC}$ for the particle size 138 nm, where $r_{eff,L,SC}$ was kept constant. However, the evaluation revealed contradictory results (calculated high values for S_{detect} but low values for DE_{max}) due to a strong dependence on the exact amount of doubly charged particles. Thus, the results of these curve-fits are not included in the further evaluation.

The values of these three parameters (i.e. $x_{0,SC}$, σ_{SC}, and $A_{scan,SC}$) were used in the fifth iteration of the SOM A ($d_{va} = 91$ nm, see Fig. S9) together with a value for $r_{eff,L,SC}$, which was also obtained using relative intensity of Mie scattering for calculation. For this particle size, the curve-fitting was performed individually for the measurement on PDU1 and PDU2. Since the curve-fitting of the measurement at PDU1 showed three peaks and the curve-fitting of the measurement at PDU2 delivered unreasonably high values, the results of these both fits are not included in the further evaluation.

Simultaneously to the measurements with AN particles at the detection units PDU1 and PDU2 of the ERICA-LAMS, the mean mass concentration of AN $\bar{C}_{NO3}$ was also determined with the ERICA-AMS (Setup B, see Fig. S7) and additionally, as a reference, the mean particle number concentration $\bar{c}_{ref}$ was measured with the CPC (methodology similar to Liu et al. (2007)). An example is provided in Fig. S11. The detection efficiency of the particle mass detection at the ERICA-AMS $DE_{vaporizer}$ is given by:

$$DE_{vaporizer} = \frac{\bar{C}_{NO3}}{\frac{1}{6} \cdot \pi \cdot \rho_{AN} \cdot S \cdot \bar{c}_{ref} \cdot \left(\left(d_{mob}{}^3 \cdot f_{SC} \right) + \left(d_{mob,DC}{}^3 \cdot f_{DC} \right) \right)} \tag{S15}$$

Here, ρ_{AN} is the density of AN, S is the Jayne shape factor and d_{mob} is the mobility diameter set at the DMA. This can be converted into the vacuum aerodynamic diameter d_{va} (see Eq. (S3)), which is used hereafter. Furthermore, the fractions of singly and doubly charged particles, f_{SC} and f_{DC}, are considered (see Table S7).

Similar to the measurements on the detection units, the particle beam parameters were obtained by curve-fittings. For these, Eq. (S16) was used. As in Eq. (S14), f_{SC} and f_{DC} were considered. However, the detection efficiency at the ERICA-AMS vaporizer does not depend on the effective laser radius ($r_{eff,L,SC}$ and $r_{eff,L,DC}$), but on the effective vaporizer radius ($r_{eff,V,SC}$ and $r_{eff,V,DC}$). This is the area where particles get vaporized in such a degree that enough ions are accelerated into the mass spectrometer to generate a detectable signal at the MCPs.

$$DE_{AMS}(x_{pos}) =$$
$$\left(\frac{1}{2} \cdot \left(erf \left(\frac{x_{pos} + r_{eff,V,SC} - x_{0,SC}}{\sqrt{2}\,\sigma_{SC}} \right) - erf \left(\frac{x_{pos} - r_{eff,V,SC} - x_{0,SC}}{\sqrt{2}\,\sigma_{SC}} \right) \right) \cdot A_{scan,SC} \cdot f_{SC} \right)$$
$$+ \left(\frac{1}{2} \cdot \left(erf \left(\frac{x_{pos} + r_{eff,V,DC} - x_{0,DC}}{\sqrt{2}\,\sigma_{DC}} \right) - erf \left(\frac{x_{pos} - r_{eff,V,DC} - x_{0,DC}}{\sqrt{2}\,\sigma_{DC}} \right) \right) \cdot A_{scan,DC} \cdot f_{DC} \right) \tag{S16}$$

The procedure for determining the individual parameters $x_{0,SC}$, σ_{SC}, $r_{eff,V,SC}$, and $A_{scan,SC}$ is the same iterative procedure as for the measurements at the detection units PDU1 and PDU2 (see Fig. S9) with Eq. (S16) instead of Eq. (S14).

The curve-fitting of the measurement at the particle size of 91 nm only provided reasonable values if the value for $r_{eff,V,SC}$ =1.98 mm was kept constant during the curve-fitting. This value was determined by averaging the $r_{eff,V,SC}$ values of the measurements for the four larger particle sizes (138 nm to 335 nm). The results of the curve-fittings for particle sizes larger than 335 nm are not suitable for further evaluation, although the measurements are meaningful in terms of amplitude and shape. As the particle beam emerges into the vacuum chamber from the ADL together with a residual air stream, the largest beam spread can be expected for the smallest particles, i.e., those sizes which are covered here. In the case of ADL position scan measurements, either at the PDUs or at the ERICA-AMS vaporizer, assuming a flat-top curve, i.e., a plateau, for an ADL position scan, the parameter A_{scan} is strongly correlated either with the effective laser radius, $r_{eff,L}$ or $r_{eff,L,SC}$, or with the effective vaporizer radius $r_{eff,V,SC}$. A plateau indicates a narrow particle beam with respect to the effective widths. In Sect. 3, only the SC subscripted values $r_{eff,L,SC}$, $r_{eff,V,SC}$, σ_{SC}, $x_{0,SC}$, and $A_{scan,SC}$ from the AN measurements (Eqs. (S14) and (S16)) were used for presentation (without subscript SC).

S4.3 Determination of the singly and doubly charged particle fraction

The parameters f_{SC} and f_{DC}, used for the fitting routines (according to Eqs. (S14) and (S16)) and the calculation of $DE_{vaporizer}$ (according to Eq. (S15)), are determined by CPC measurements during the experiments. Here, the ratio of the charge fraction of doubly charged (DC) particles to singly charged (SC) particles (DC charge fraction/SC charge fraction) φ for the respective particle size was adopted. The values of the DC charge fraction and the SC charge fraction were read out from Tigges et al. (2015).

The procedure is iterative, starting with the second largest scan number s ($s = 4$ in SOM A and $s = 2$ in SOM B; see Table S8). For the largest particle sizes used here ($s = 5$ in SOM A and $s = 3$ in SOM B) it is assumed that $f_{DC} = 0$ and $f_{SC} = 1$, since particle sizes larger than 1000 nm are only produced in very low numbers.

The parameter $f_{DC,s}$ is the f_{DC} value for the scan number s and is iteratively calculated separately for each SOM:

$$f_{DC,s} = \frac{c_{DC,s}}{\bar{c}_{tot,s}} = \frac{\varphi_{s+1} \cdot c_{SC,s+1}}{\bar{c}_{tot,s}} \tag{S17}$$

Here, $f_{DC,s}$ is the fraction of the doubly charged particles, φ_{s+1} is the DC charge fraction to SC charge fraction ratio for scan number $s + 1$, read out from Tigges et al. (2015), $c_{DC,s}$ is the number concentration of the doubly charged particles for scan number s, $c_{SC,s+1}$ is the number concentration of the singly charged particles for scan number $s + 1$, and $\bar{c}_{tot,s}$ is the average of the total CPC number concentration for scan number s.

$c_{SC,s+1}$ cannot be measured directly. Since no higher than double charges have to be considered:

$$c_{SC,s+1} = (\bar{c}_{tot,s+1} - c_{DC,s+1}) \tag{S18}$$

Here, $c_{DC,s+1}$ is the number concentration of the doubly charged particles for scan number $s + 1$, and $\bar{c}_{tot,s+1}$ is the average of the total CPC number concentration for scan number $s + 1$.

Table S8: Scan numbers s of the measured AN particles for various particle sizes of singly charged species (SC) d_{va}, the corresponding DC charge fraction /SC charge fraction ratios φ according to Tigges et al. (2015), and the calculated fractions of singly f_{SC} and doubly charged f_{DC} particles for the two series of measurements (SOM) A and B.

scan number s	d_{va} in nm	φ	f_{SC}	f_{DC}	SOM
1	91		0.887	0.113	A
2	138	0.171	0.877	0.123	
3	213	0.302	0.892	0.108	
4	335	0.460	0.937	0.063	
5	548	0.631	1.000	0.000	
1	297		0.964	0.036	B
2	483	0.585	0.982	0.018	
3	814	0.747	1.000	0.000	

Since no higher than double charges have to be considered, the value for f_{SC} of the size number s ($f_{SC,s}$) is:

$$f_{SC,s} = 1 - f_{DC,s} \tag{S19}$$

The results for the respective values according to the scan number s for f_{SC} and f_{DC} are summarized in Table S8 and transferred to Table S7.

S4.4   ADL position scans with ammonium nitrate (AN) particles

Fig. S10 exemplarily displays the AN particle beam characterization measurement with particles of 297 nm in size at PDU1 including the curve fit pursuant Eq. (S14) (solid line). The parameters indexed with DC ($x_{0,DC}$, σ_{DC}, $r_{eff_{DC}}$, and $A_{scan,DC}$ shown in the box resulted from the curve fitting with particle size of 483 nm, which contribute as doubly charged particles. The bars for the uncertainty of the detection efficiency DE_{PDU} are based on counting statistics of the PDU and the CPC. The uncertainties of the curve fitting results of $x_{0,DC}$, σ_{DC}, $r_{eff_{DC}}$, $A_{scan,DC}$, f_{SC}, and f_{DC} appear as 0, because during curve fitting routine they were kept as constants.
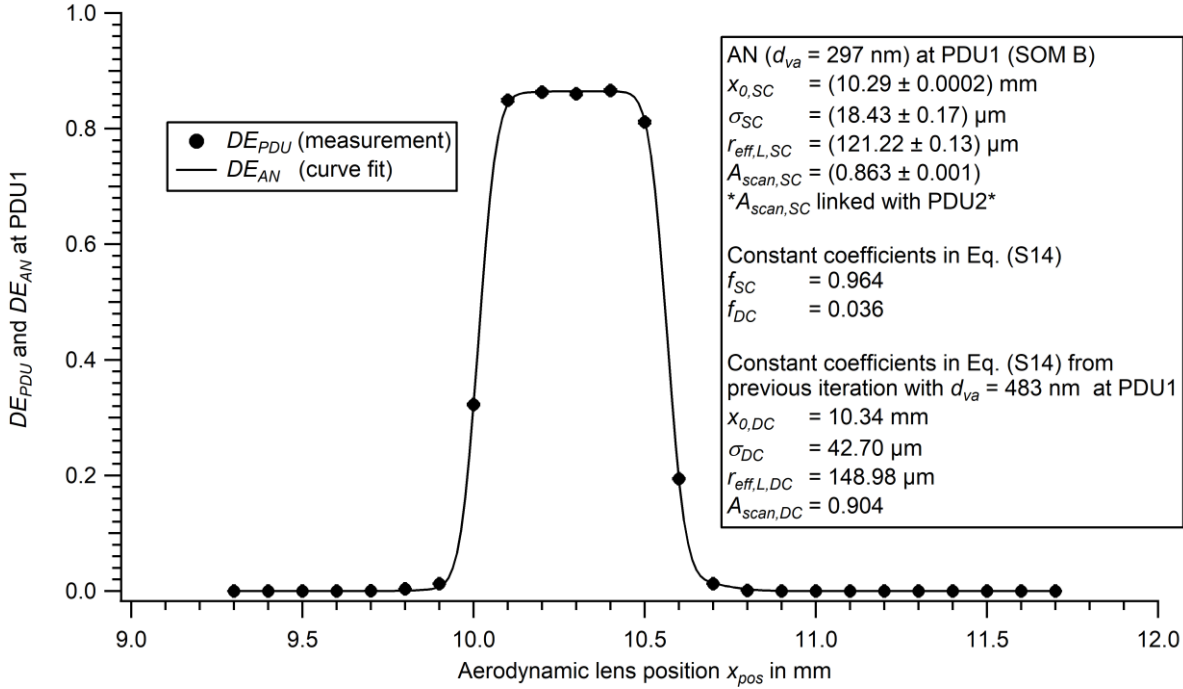
Fig. S10: Scan of the ADL position (x_{pos}) with AN particles of d_{va} = 297 nm perpendicular to the laser beam at PDU1. Displayed are the DE_{PDU} values of the measurement (markers) according to Eq. (4) and the curve fit (DE_{AN}; line) according to Eq. (S14). The results and constants of the curve fits are shown in the text box. The values of σ_{SC}, σ_{DC}, $r_{eff,L,SC}$, and $r_{eff,L,DC}$ were rescaled according to the instrument's geometry (see Sect. S1.2), using the intercept theorem. The uncertainty of the detection efficiency is based on counting statistics of the PDU and the CPC and the uncertainty of the lens position results from reading errors. The uncertainty bars are in all cases smaller than the symbol.

Fig. S11 shows the detection efficiency $DE_{vaporizer}$ and DE_{AMS} of AN particles for different ADL positions (x_{pos}). $DE_{vaporizer}$ was evaluated from Eq. (S15) and curve fitted with the function according to Eq. (S16). The parameters $x_{0,DC}$, σ_{DC}, $r_{L,DC}$, and $A_{scan,DC}$ were taken from the corresponding measurement with particle size of 483 nm, representing the size of doubly charged particles of 297 nm in size. The bars for the uncertainty of the detection efficiency $DE_{vaporizer}$ are based on the counting statistics of the CPC as well as the estimated counting statistics expected at the ERICA-AMS. Additionally, the noise of the filter measurement was considered. $x_{0,DC}$, σ_{DC}, $r_{eff_{DC}}$, $A_{scan,DC}$, f_{SC}, and f_{DC} were kept constant and thus appear to have no uncertainty. The wide plateau of the profile is caused by the well-defined edges of the vaporizer.
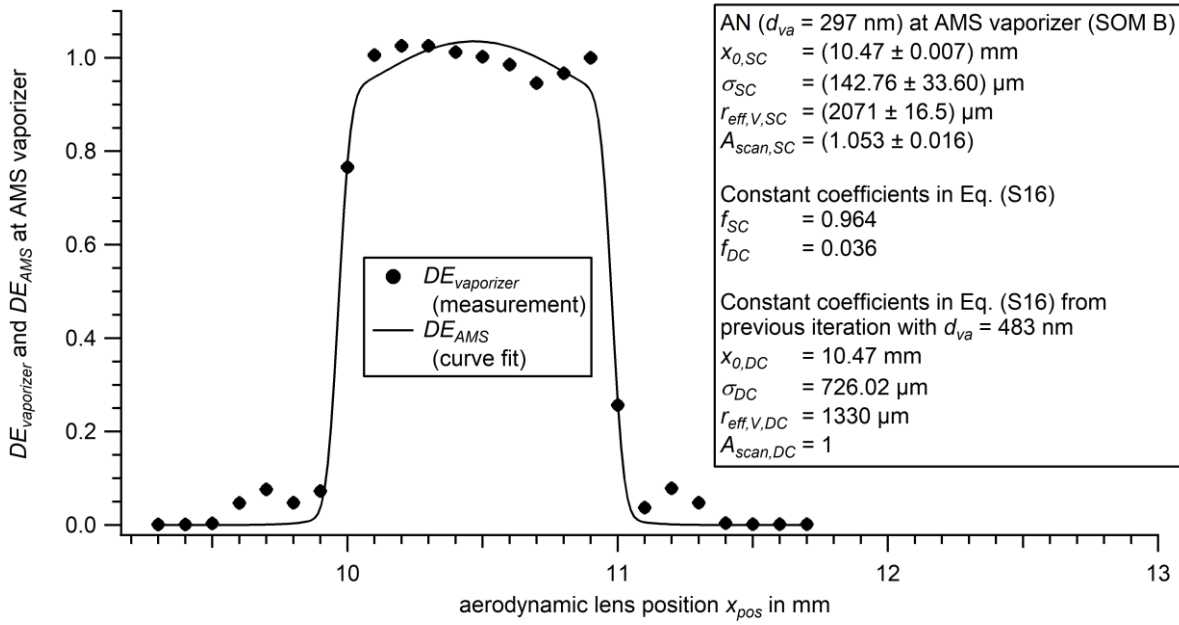
Fig. S11: Scan of the ADL position (x_{pos}) with AN particles of d_{va} = 297 nm at the ERICA-AMS vaporizer. The particle mass detection efficiency $DE_{vaporizer}$ was evaluated from Eq. (S15) (markers) and curve fitted (DE_{AMS}; line) with a function according to Eq. (S16). The results and constants of the curve fits are shown in the text box. The values of σ_{SC}, σ_{DC}, $r_{eff,V,SC}$, and $r_{eff,V,DC}$ were rescaled according to the instrument's geometry (see Sect. S1.2), using the intercept theorem. The uncertainty of the detection efficiency is based on counting statistics of the CPC as well as the estimated counting statistic expected for the ERICA-AMS. The uncertainty of the lens position results from reading errors. The uncertainty bars are in all cases smaller than the symbol.

S4.5 Determination of maximum detection efficiency DE_{max} and the detection efficiency for the field deployment in Kathmandu DE_{KTM}

The parameters that are needed to determine DE_{max} and DE_{KTM} (see Sect. 3.3.3) were obtained from curve fittings (see Sects. 3.3.2 and S4.2). The corresponding equations for all efficiencies are comprehended here:

5 Determination of DE_{max} for PSL particles at PDU1 and PDU2:

$$DE_{max} = \frac{1}{2} \cdot \left(erf\left(\frac{x_{pos} + r_{eff,L} - x_0}{\sqrt{2}\sigma} \right) - erf\left(\frac{x_{pos} - r_{eff,L} - x_0}{\sqrt{2}\sigma} \right) \right) \cdot A_{scan} \qquad (S20)$$

Determination of DE_{max} for AN particles at PDU1 and PDU2:

$$DE_{max} =$$
$$\left(\frac{1}{2} \cdot \left(erf\left(\frac{x_{pos} + r_{eff,L,SC} - x_{0,SC}}{\sqrt{2}\,\sigma_{SC}} \right) - erf\left(\frac{x_{pos} - r_{eff,L,SC} - x_{0,SC}}{\sqrt{2}\,\sigma_{SC}} \right) \right) \cdot A_{scan,SC} \right) \qquad (S21)$$

Determination of DE_{max} for AN particles at the ERICA-AMS:

$$DE_{max} =$$
$$\left(\frac{1}{2} \cdot \left(erf\left(\frac{x_{pos} + r_{eff,V,SC} - x_{0,SC}}{\sqrt{2}\,\sigma_{SC}} \right) - erf\left(\frac{x_{pos} - r_{eff,V,SC} - x_{0,SC}}{\sqrt{2}\,\sigma_{SC}} \right) \right) \cdot A_{scan,SC} \right) \qquad (S22)$$

Determination of DE_{KTM} for PSL particles at PDU1 and PDU2, where $x_{pos} = 10.55$ mm:

$$DE_{KTM} = \frac{1}{2} \cdot \left(erf\left(\frac{10.55 + r_{eff,L} - x_0}{\sqrt{2}\sigma} \right) - erf\left(\frac{10.55 - r_{eff,L} - x_0}{\sqrt{2}\sigma} \right) \right) \cdot A_{scan} \qquad (S23)$$

Determination of DE_{KTM} for AN particles at PDU1 and PDU2, where $x_{pos} = 10.55$ mm:

$$DE_{KTM} =$$
$$\left(\frac{1}{2} \cdot \left(erf\left(\frac{10.55 + r_{eff,L,SC} - x_{0,SC}}{\sqrt{2}\,\sigma_{SC}} \right) - erf\left(\frac{10.55 - r_{eff,L,SC} - x_{0,SC}}{\sqrt{2}\,\sigma_{SC}} \right) \right) \cdot A_{scan,SC} \right) \qquad (S24)$$

15 Determination of DE_{KTM} for AN particles at the ERICA-AMS, where $x_{pos} = 10.55$ mm:

$$DE_{KTM} =$$
$$\left(\frac{1}{2} \cdot \left(erf\left(\frac{10.55 + r_{eff,V,SC} - x_{0,SC}}{\sqrt{2}\,\sigma_{SC}} \right) - erf\left(\frac{10.55 - r_{eff,V,SC} - x_{0,SC}}{\sqrt{2}\,\sigma_{SC}} \right) \right) \cdot A_{scan,SC} \right) \qquad (S25)$$

S4.6 Particle beam characteristics

S4.6.1 Scaling parameter A_{scan}
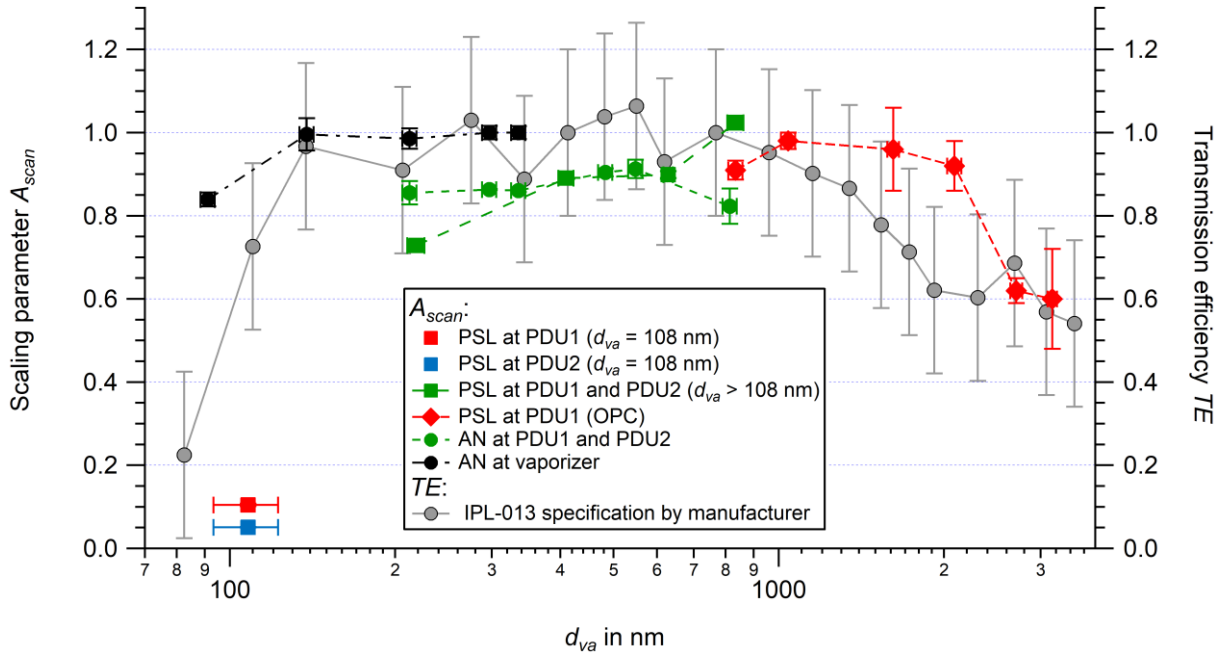
Fig. S12: The scaling parameter A_{scan} (left ordinate) as a function of particle size d_{va} for PSL (squares) and AN (circles) particles
measured at the detection units PDU1 (red), PDU2 (blue), and both (PDU1 and PDU2, green), AN particles at the ERICA-AMS
vaporizer (black). The reference values for number concentrations were either obtained from the experimental setup with the CPC
or the OPC (Setup B or C, respectively, see Fig. S7). The IPL-013 specification transmission efficiency (TE) curve (data provided by
manufacturer Aerodyne Research Inc.) is plotted in gray (right ordinate) as a function of particle size d_{va}. The PSL particle
measurements with sizes of 108 nm were evaluated not by a combined curve-fitting procedure but individually (see red and blue
symbol in the lower left corner). The uncertainties of A_{scan} result from the curve-fitting (one standard deviation). The uncertainty
of TE is ±0.2 and was estimated from the uncertainties presented in Peck et al. (2016). The uncertainty of PSL particle size is given
by NIST certificates and converted to d_{va}. The uncertainty of AN particle size d_{va} is estimated to be 3 % (Hings, 2006). These
uncertainties for PSL and AN particle sizes are the same for Fig. S12 up to Fig. S14. The error bars are in some cases smaller than
the symbol.

One parameter provided by the curve-fitting functions (Eq. (5), and Eqs. (S14) and (S16)) is the scaling parameter A_{scan}. The

parameter A_{scan} represents the difference of the scan peak value maximum to 100 %. As mentioned above (see Sect. 3.3.1)

A_{scan} is largely affected by the transmission efficiency of the ADL. In Fig. S12, the parameter A_{scan} is plotted together with

the transmission efficiency TE as specified by the manufacturer (Aerodyne) as a function of the particle size d_{va}.

Due to the combined curve-fitting procedure described in Sect. 3.3.1, the value of A_{scan} at PDU1 equals the value at PDU2

for each particle type and size. This is the case for all AN particle measurements and for all PSL particle measurements for

particle sizes larger than 108 nm. Since the evaluation of the measurement with PSL particles of 108 nm in size was not

conducted by a combined curve-fitting routine, two values of A_{scan} are available for one PSL particle size (see Sect. 3.3.1). In

contrast to particle sizes larger than 108 nm, for particles of 108 nm in size, the particle beam width is broader than the effective

laser width (see Fig. 6 in 3.3.2). This presumably is the case along the laser beam axis and not only along the scan direction.

This circumstance leads to detection losses of particles, which are even higher for PDU2 than for PDU1, due to the particle

beam divergence, and indicates that the A_{scan} values determined for the detection units for PSL particles of 108 nm in size are

limited by the optical detection, rather than the TE of the ADL (0.10 at PDU1 and 0.05 at PDU2 for PSL particles). For the

measurements with particles larger than 108 nm in size, the parameter A_{scan} increases with particle size and reaches a

maximum value of 1 for PSL particles of 834 nm in size. For the measurements with particles larger than 834 nm in size, A_{scan}

decreases.

The values of A_{scan} determined by measurements at the vaporizer of the ERICA-AMS are not directly comparable to the

values of the measurements at the PDUs, due to the freedom of determining the ionization efficiency (IE) calibration factor

(see Sect. 3.6.2) at the ERICA-AMS. Thus, the maximum A_{scan} value, for a particle size of 335 nm, was normalized to 1. A decrease of A_{scan} is obtained for particles of 91 nm in size.

The parameter A_{scan} can be used as an approximation to describe the ADL transmission efficiency TE as used by Molleker et al. (2020) for the ERICA. The data of the gray curve (TE) was provided by the manufacturer (Aerodyne Inc.) in the datasheet

5 of the here applied ADL model (IPL-013). It shows the TE of the ADL deployed in the ERICA. A good agreement between A_{scan} and the specified TE is achieved by means of optical particle detection for particle sizes between 200 nm and 3000 nm. The here-used ADL type was comprehensively described by Peck et al. (2016) and Xu et al. (2017). Xu et al. (2017) show that the TE is above 0.80 in a size range between 200 nm and 2000 nm reaching a maximum of 1 in the size range between 300 nm and 1000 nm. This is slightly higher than what was achieved in the measurements here presented. A reason might be the

10 different method for determination of A_{scan} (here) and of TE by Xu et al. (2017). The d_{50} cut-offs of the TE are reported for particle sizes between ~120 nm and 3.5 µm (Xu et al., 2017). For PSL and AN, the A_{scan} values were found to be above 0.7 for the size range between 200 nm and 2090 nm and above 0.6 for particle sizes up to 3150 nm. For the lower size cut-off, the measurement with the AMS has to be considered. The rather stable values of A_{scan} for particle sizes between 138 nm and 335 nm agrees well with the specified values of TE. For a particle size of 91 nm, however, A_{scan} is above the specified value of

15 TE, probably indicating a lower d_{50} cut-off than specified.

Overall, the ADL deployed is suitable to transmit the accumulation mode and partly the coarse mode of the ambient aerosol. A_{scan} is a reasonable measure of the TE for large particle sizes (larger than 200 nm) at the PDUs by optical means, but not for smaller particle sizes. For particle sizes smaller than 200 nm, the measurements at the ERICA-AMS are more suitable to estimate the TE, however, no d_{50} cut-offs can be obtained from these measurements.

S4.6.2 Particle beam shift $x_{0,shift}$

During the development of the instrument, it was found that the particle beam cross-sectional profiles for all particle sizes appear as non-concentric as indicated by various x_0 values. This deviation of the various x_0 values from the adjusted particle beam axis center is termed particle beam shift $x_{0,shift}$. To quantify the deviation of the various modal values x_0 from the

25 adjusted axis center (x_{pos} = 10.55 mm) at the location of PDU1 and PDU2, the value x_{pos} = 10.55 mm was subtracted from the x_0 values as determined by the curve-fitting procedures. After this calculation, the distance ratios in the geometry of the instrument (see Sect. S1.2) were considered for both locations. In Fig. S13, the parameter $x_{0,shift}$ is plotted versus the particle size d_{va} for PSL and AN particles. The maximum value of $x_{0,shift}$ is 0.21 mm at PDU2 (d_{va} = 834 nm) for PSL particles and 0.62 mm for AN particles at the vaporizer (d_{va} = 138 nm).

30 After the described lens rotation (see Sect. S3), which occurred after the StratoClim campaign and after the characterization measurements presented in Sect. 3.3, we found that the overall particle beam cross-sectional area does not describe a circle but an oval shape. By that rotation, $x_{0,shift}$ appears to be reduced. This observation is part of further investigations and, since the condition during the StratoClim campaign is described here, is not part of this publication.
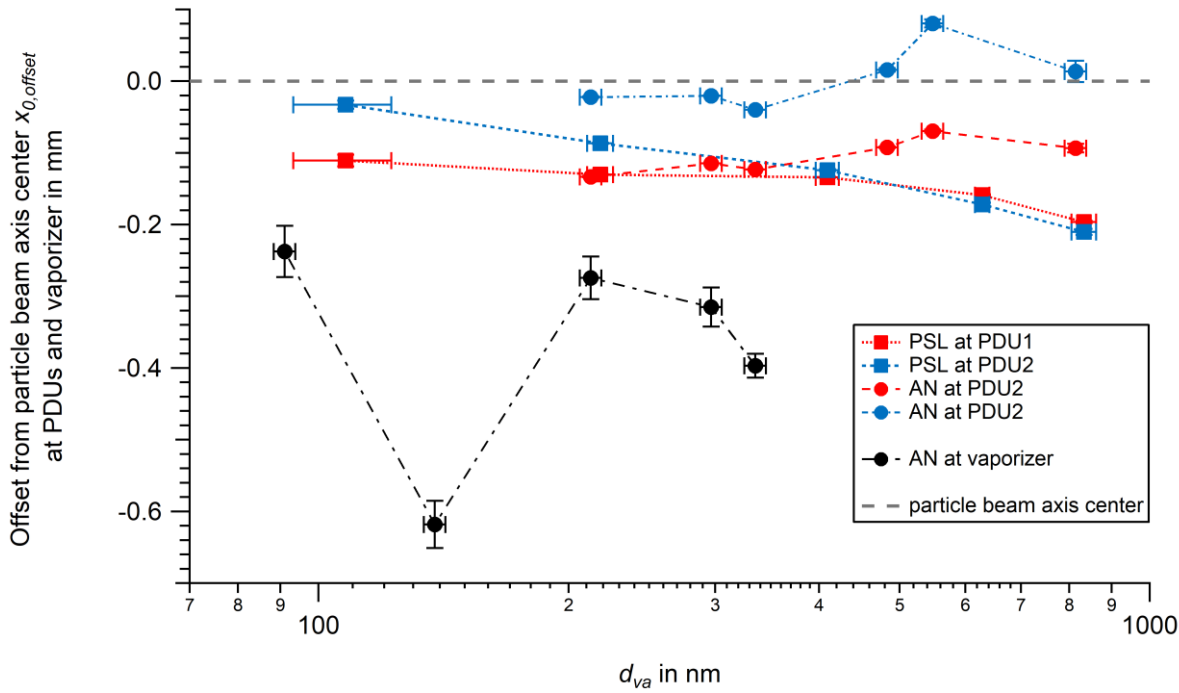
Fig. S13: The deviation of the various modal values x_0 from the adjusted particle beam axis center (x_{pos} = 10.55 mm; dark gray horizontal dashed line) at the location of PDU1 and PDU2 (termed $x_{0,shift}$) as a function of particle size d_{va} for PSL (squares) and AN (circles) particles measured at PDU1 (red) and PDU2 (blue), and for AN particles measured at the ERICA-AMS vaporizer (black). Uncertainties of $x_{0,shift}$ result from the curve-fittings (one standard deviation). The uncertainty of PSL particle size d_{va} is given by NIST certificates. The uncertainty of AN particle size d_{va} is estimated to be 3 % (Hings, 2006). The error bars are in some cases smaller than the symbol.

S4.6.3 Particle beam divergence α

The particle beam divergence α is displayed in Fig. S14 for various PSL and AN particle sizes, at both detection stages (PDU1 and PDU2), and at the ERICA-AMS vaporizer, calculated from the particle beam width analogue σ defined as:

$$\alpha = \frac{\sigma}{z_{asd}} \tag{S26}$$

The parameter σ is in the dimension of a $\frac{1}{\sqrt{e}}$-radius and z_{asd} is the distance from the adjustment screws to the ball joint of the ADL in the recipient (z_{asd} = 133.7 mm, see Sect. S1.2). It is apparent that the very small particles (d_{va} < 200 nm) diverge into a much wider cone than the other measured sizes. The reason for this is the collisional interaction with the residual air molecules right after critical expansion (Huffman et al., 2005). The values at PDU1 are larger than for the values at PDU2 for small particles. One reason is the fact that these particle sizes do not have a common, single starting point but rather a finite starting area within the cross-section of the lens's exit. This fact might be caused by turbulence in the ADL and leads to a discrepancy of the different divergence values for the same particle sizes at different distances from the ADL's exit. Values of α measured at PDU2 are more reliable than those measured at PDU1, since the influence of the initial conditions within the starting area is higher for measurements closer to the ADL, i.e., measurements at PDU1, than for measurements further from the ADL, i.e., measurements at PDU2 and at the vaporizer. This is especially the case for the measurements with PSL particles of 108 nm in size. Larger particle sizes (d_{va} > 421 nm) tend to slightly higher α values. For particle sizes between 218 nm and 834 nm, the particle beam divergence α seems to be independent of the particle type. A minimum for α of 0.1 mrad can be extracted from the measurements with AN particles of 335 nm in size at PDU2 and a maximum of 4.6 mrad for PSL particles of 108 nm in size at PDU1.

The measurements with the OPC as reference device were obtained before the ADL rotation (see Sect. S3). However, considering a rotationally symmetric particle beam profile for each specific particle size, the divergence is unaffected by the ADL rotation. The values for these measurements are between 1.1 mrad and 1.7 mrad.
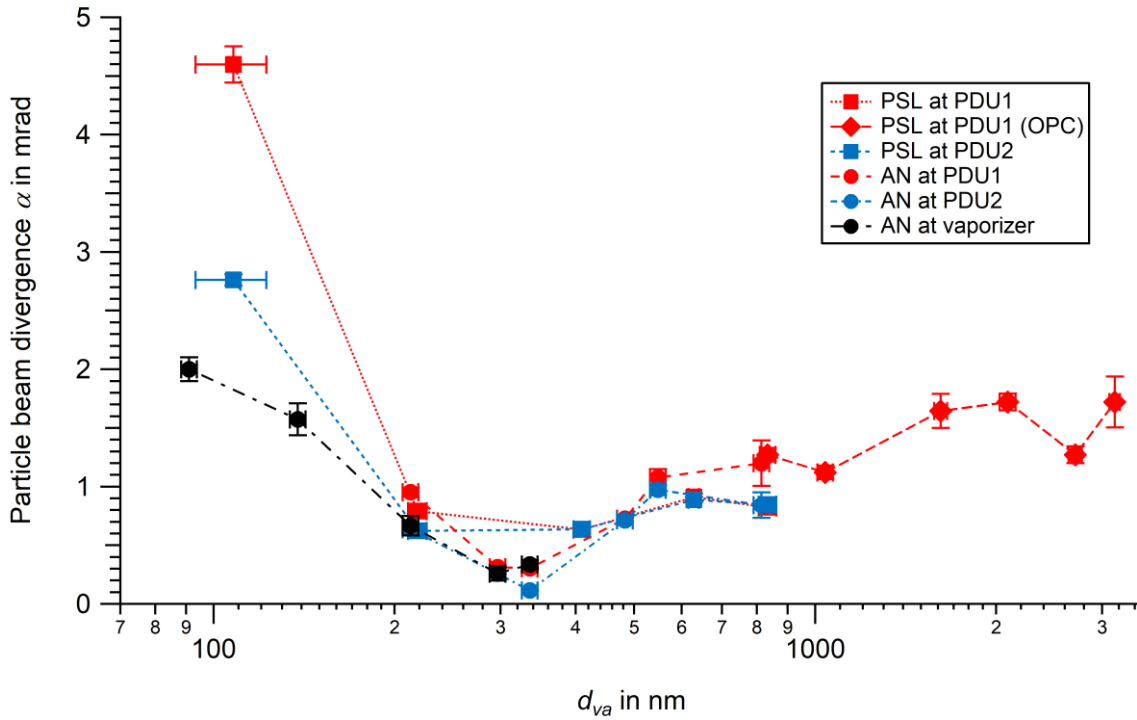
Fig. S14: The particle beam divergence α as a function of particle size d_{va} for PSL (squares) and AN (circles) particles measured at the detection units PDU1 (red) and PDU2 (blue), and for AN particles measured at the ERICA-AMS vaporizer (black). The reference values for number concentrations were either obtained from the experimental setup with the CPC or the OPC (Setup B or C, respectively, see Fig. S7). Values of α measured at PDU2 are more reliable than those measured at PDU1 (see text). The uncertainties of α result from the curve fitting (one standard deviation) and reading errors. The uncertainty of PSL particle size d_{va} is given by NIST certificates. The uncertainty of AN particle size d_{va} is estimated to be 3 % (Hings, 2006). The uncertainty bars are in some cases smaller than the symbol.

S5   Mass resolution of the ERICA-AMS

Fig. S15 displays the mass resolution $R_{MS} = m/\varDelta m$ as function of the m/z-ratio for the ERICA-AMS calculated by the evaluation software "Tofware". This is comparable for a commercial C-ToF-MS from Aerodyne (DeCarlo et al., 2006).
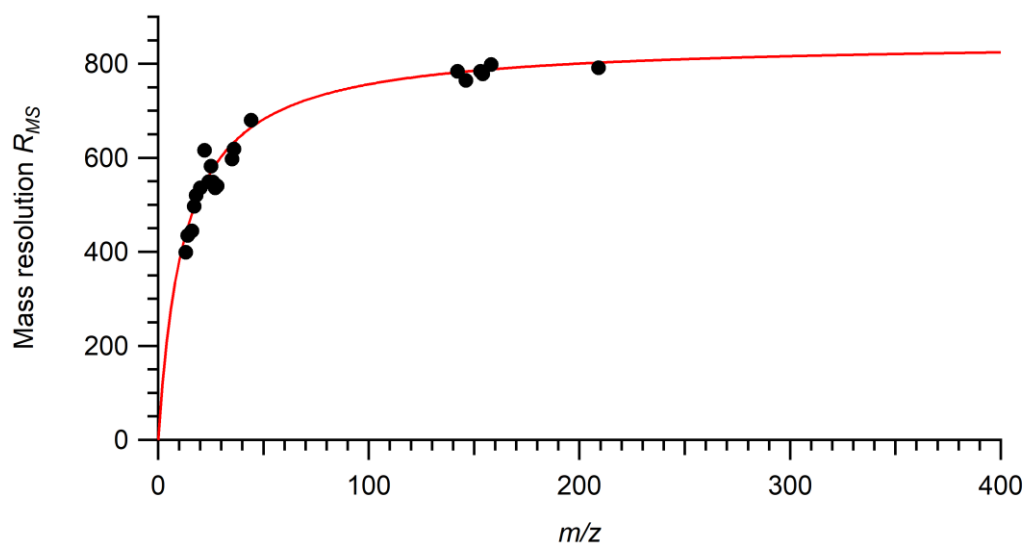
5   **Fig. S15: Mass resolution R_{MS} of the ERICA-AMS spectrum fitted through the largest peaks.**

S6   Mean spectrum of meteoric material containing single particles

As identified and described by Murphy et al. (1998) and Cziczo et al. (2001), the meteoric material containing particle type is characterized by a high abundance of magnesium (Mg^+, isotopes at m/z 24, m/z 25, and m/z 26) and iron (Fe^+, isotopes at m/z 56 and m/z 54) signals in the cation spectrum and of sulfate (HSO_4^- at m/z -97) in the anion spectrum. In Fig. S16, the mean spectrum of the meteoric material-containing particle type, including 956 mass spectra measured during one research flight, is shown. Also sodium (Na^+, m/z 23), aluminum (Al^+, m/z 27), and calcium signals (Ca^+, m/z 40) as well as other sulfate fragments, such as SO_3^- (m/z -80), SO_4^- (m/z -96), $H^{34}SO^-$ (m/z -99), $HSO_4SO_3^-$ (m/z -177), $HSO_4SO_4^-$ (m/z -193), and $H_2SO_4HSO_4^-$ (m/z -195) can be found in the mean spectrum. In the mass spectra of this particle type recorded with ERICA-LAMS, a signal at m/z -44, suspected as SiO^-, is present.
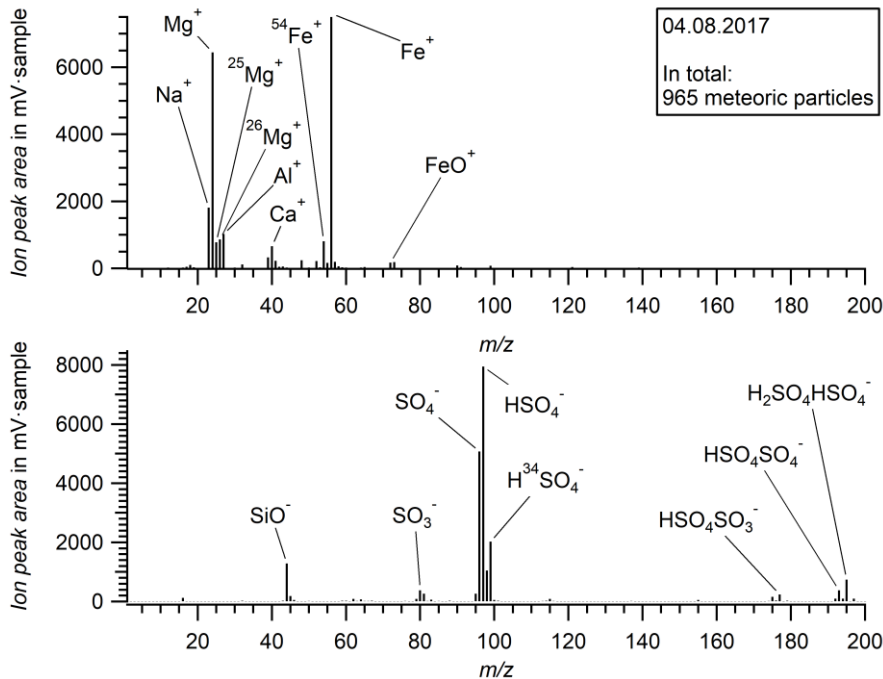
Fig. S16: Mean spectrum of 956 meteoric material containing single particles recorded during a research flight on 04.08.2017 during StratoClim in Nepal.

References

Allen, M. D., and Raabe, O. G.: Slip Correction Measurements of Spherical Solid Aerosol Particles in an Improved Millikan Apparatus, Aerosol Sci. Technol., 4, 269-286, https://doi.org/10.1080/02786828508959055, 1985.

Bohren, C. F., and Huffman, D. R.: Absorption and scattering of light by small particles, Wiley science paperback series, New York, NY, USA a.o., 1998.

Cziczo, D. J., Thomson, D. S., and Murphy, D. M.: Ablation, Flux, and Atmospheric Implications of Meteors Inferred from Stratospheric Aerosol, Science, 291, 1772-1775, https://doi.org/10.1126/science.1057737, 2001.

DeCarlo, P. F., Slowik, J. G., Worsnop, D. R., Davidovits, P., and Jimenez, J. L.: Particle Morphology and Density Characterization by Combined Mobility and Aerodynamic Diameter Measurements. Part 1: Theory, Aerosol Sci. Technol., 38, 1185-1205, https://doi.org/10.1080/027868290903907, 2004.

DeCarlo, P. F., Kimmel, J. R., Trimborn, A., Northway, M. J., Jayne, J. T., Aiken, A. C., Gonin, M., Fuhrer, K., Horvath, T., Docherty, K. S., Worsnop, D. R., and Jimenez, J. L.: Field-Deployable, High-Resolution, Time-of-Flight Aerosol Mass Spectrometer, Anal. Chem., 78, 8281-8289, https://doi.org/10.1021/ac061249n, 2006.

Dragoneas, A., Molleker, S., Appel, O., Hünig, A., Böttger, T., Hermann, M., Drewnick, F., Schneider, J., Weigel, R., and Borrmann, S.: The realization of autonomous, aircraft-based, real-time aerosol mass spectrometry in the stratosphere, Atmos. Meas. Tech., in preparation, n/a, 2021.

Eichler, H. J., Kronfeldt, H.-D., and Sahm, J.: Das neue Physikalische Grundpraktikum, 3rd edition ed., Springer-Lehrbuch, Springer, Berlin and Heidelberg, Germany, 2016.

Galpin, T., Chartier, R. T., Levergood, N., and Greenslade, M. E.: Refractive index retrievals for polystyrene latex spheres in the spectral range 220–420 nm, Aerosol Sci. Technol., 51, 1158-1167, https://doi.org/10.1080/02786826.2017.1339014, 2017.

Hinds, W. C.: Aerosol technology: properties, behavior, and measurement of airborne particles, 2nd edition ed., Wiley, New York, NY, USA, XX, 483 pp., 1999.

Hings, S.: Characterisation and Field Deployment of a Novel Quantitative Time-of-Flight Aerosol Mass Spectrometer (ToF-AMS), PhD thesis, Johannes Gutenberg-Universität Mainz, Mainz, Germany, https://doi.org/10.25358/openscience-3333, 2006.

Huffman, J. A., Jayne, J. T., Drewnick, F., Aiken, A. C., Onasch, T., Worsnop, D. R., and Jimenez, J. L.: Design, Modeling, Optimization, and Experimental Tests of a Particle Beam Width Probe for the Aerodyne Aerosol Mass Spectrometer, Aerosol Sci. Technol., 39, 1143-1163, https://doi.org/10.1080/02786820500423782, 2005.

Hünig, A.: Development, characterization, and first field deployments of a novel aerosol mass spectrometer combining laser ablation and flash vaporization techniques for aircraft application at high altitudes, PhD thesis, Johannes Gutenberg-Universität Mainz, Mainz, Germany, https://doi.org/10.25358/openscience-5554, 2021.

Jayne, J. T., Leard, D. C., Zhang, X., Davidovits, P., Smith, K. A., Kolb, C. E., and Worsnop, D. R.: Development of an Aerosol Mass Spectrometer for Size and Composition Analysis of Submicron Particles, Aerosol Sci. Technol., 33, 49-70, https://doi.org/10.1080/027868200410840, 2000.

Jimenez, J. L., Bahreini, R., Cocker, D. R., Zhuang, H., Varutbangkul, V., Flagan, R. C., Seinfeld, J. H., O'Dowd, C. D., and Hoffmann, T.: New particle formation from photooxidation of diiodomethane (CH2I2), J. Geophys. Res.-Atmos., 108, https://doi.org/10.1029/2002JD002452, 2003a.

Jimenez, J. L., Bahreini, R., Cocker, D. R., Zhuang, H., Varutbangkul, V., Flagan, R. C., Seinfeld, J. H., O'Dowd, C. D., and Hoffmann, T.: Correction to "New particle formation from photooxidation of diiodomethane (CH2I2)", J. Geophys. Res.-Atmos., 108, https://doi.org/10.1029/2003JD004249, 2003b.

Liu, P. S. K., Deng, R., Smith, K. A., Williams, L. R., Jayne, J. T., Canagaratna, M. R., Moore, K., Onasch, T. B., Worsnop, D. R., and Deshler, T.: Transmission Efficiency of an Aerodynamic Focusing Lens System: Comparison of Model Calculations and Laboratory Measurements for the Aerodyne Aerosol Mass Spectrometer, Aerosol Sci. Technol., 41, 721-733, https://doi.org/10.1080/02786820701422278, 2007.

Molleker, S., Helleis, F., Klimach, T., Appel, O., Clemen, H.-C., Dragoneas, A., Gurk, C., Hünig, A., Köllner, F., Rubach, F., Schulz, C., Schneider, J., and Borrmann, S.: Application of an O-ring pinch device as a constant pressure inlet (CPI) for airborne sampling, Atmos. Meas. Tech., 2020, 1-13, https://doi.org/10.5194/amt-2020-66, 2020.

5   Murphy, D. M., Thomson, D. S., and Mahoney, M. J.: In Situ Measurements of Organics, Meteoritic Material, Mercury, and Other Elements in Aerosols at 5 to 19 Kilometers, Science, 282, 1664-1669, https://doi.org/10.1126/science.282.5394.1664, 1998.

Peck, J., Gonzalez, L. A., Williams, L. R., Xu, W., Croteau, P. L., Timko, M. T., Jayne, J. T., Worsnop, D. R., Miake-Lye, R. 10   C., and Smith, K. A.: Development of an aerosol mass spectrometer lens system for PM2.5, Aerosol Sci. Technol., 50, 781-789, https://doi.org/10.1080/02786826.2016.1190444, 2016.

Seinfeld, J. H., and Pandis, S. N.: Atmospheric chemistry and physics : from air pollution to climate change, 3rd edition ed., A Wiley-Interscience publication, Wiley, Hoboken, NJ, USA, 1152 pp., 2016.

Tigges, L., Wiedensohler, A., Weinhold, K., Gandhi, J., and Schmid, H. J.: Bipolar charge distribution of a soft X-ray diffusion charger, J. Aerosol Sci, 90, 77-86, https://doi.org/10.1016/j.jaerosci.2015.07.002, 2015.

Vetter, T.: Berechnung der Mie-Streufunktionen zur Kalibrierung optischer Partikelzähler, diploma thesis, Johannes 20   Gutenberg-Universität Mainz, Mainz, Germany, 2004.

Wiedensohler, A.: An approximation of the bipolar charge distribution for particles in the submicron size range, J. Aerosol Sci, 19, 387-389, https://doi.org/10.1016/0021-8502(88)90278-9, 1988.

25   Xu, W., Croteau, P., Williams, L., Canagaratna, M., Onasch, T., Cross, E., Zhang, X., Robinson, W., Worsnop, D., and Jayne, J.: Laboratory characterization of an aerosol chemical speciation monitor with PM2.5 measurement capability, Aerosol Sci. Technol., 51, 69-83, https://doi.org/10.1080/02786826.2016.1241859, 2017.

Zapp, K.-H., Wostbrock, K.-H., Schäfer, M., Sato, K., Seiter, H., Zwick, W., Creutziger, R., and Leiter, H.: Ammonium 30   Compounds, Ullmann's Encyclopedia of Industrial Chemistry, https://doi.org/10.1002/14356007.a02_243, 2000.